

# Cenozoic faulting in the Upper Hyland River Valley, Southeastern Yukon: A thermochronological perspective

Joel Padgett <sup>a</sup>, Eva Enkelmann <sup>a</sup>, Dawn A. Kellett <sup>b</sup>, David P. Moynihan <sup>c</sup>, and Tobias Stephan <sup>d</sup>

<sup>a</sup>Department of Earth, Energy, and Environment, University of Calgary, Calgary, AB, Canada; <sup>b</sup>Geological Survey of Canada–Atlantic, Dartmouth, NS, Canada; <sup>c</sup>Yukon Geological Survey, Whitehorse, YT, Canada; <sup>d</sup>Department of Geology, Lakehead University, Thunder Bay, ON, Canada

Corresponding author: Joel Padgett (email: joel.padgett@ucalgary.ca)

## Abstract

The Logan fault is one of many dextral faults that strike generally parallel to the northwest trend of the Northern Canadian Cordillera. Though widely documented, the timing and magnitude of displacement on many of these orogen-parallel faults are not well-constrained. Here, we present new low-temperature thermochronology data and thermal history models from the Upper Hyland River Valley area in the Logan Mountains in southeastern Yukon that document accelerated cooling between ca. 60–50 Ma in localized regions adjacent to faults that strike obliquely to and likely connect with the Logan fault. We propose that this phase of localized cooling was driven by the activation of a network of faults in the Upper Hyland River Valley, resulting in ~4–5.5 km of local exhumation. We suggest that faulting in the Upper Hyland River Valley was synthetic with dextral slip on the Tintina fault, a lithospheric-scale structure thought to have accommodated ~430 km of dextral strike-slip.

**Key words:** thermochronology, Canadian Cordillera, faults, Yukon, apatite

## 1. Introduction

Decades of field mapping has led to the recognition of a broad network of orogen-parallel, northwest-trending, dextral strike-slip faults across the Northern Canadian Cordillera (Fig. 1) (see reviews in Gabriele et al. 2006 and Monger and Gibson 2019). These include lithospheric-scale structures such as the Tintina and Denali faults and several regional faults such as the Cassiar and Teslin faults (Figs. 1 and 2). Understanding when these structures formed, their shear sense, the amount of displacement they accommodated, and times of activation is crucial for interpreting the local geology and also the response of orogenic interiors to changing plate boundary conditions along active plate margins. Constraining the timing of fault formation and reactivation in the Northern Canadian Cordillera is challenged by the limited exposures of these faults, and hence, few direct age constraints exist for these fault systems (e.g., Mottram et al. 2020).

Field mapping in the Upper Hyland River Valley in the Logan Mountains in southeastern Yukon has led to the recognition of the northwest–southeast-trending Logan fault located ~100 km east of the Tintina fault (Fig. 2; Moynihan 2016, 2017; Yukon Geological Survey 2022). Dextral displacement is suggested by offset of mid-Cretaceous granitoids that intruded Precambrian–Paleozoic sedimentary rocks of the Selwyn fold-thrust belt (Fig. 3A). However, there are few constraints on the timing, style, and magnitude of displacement and the role of adjacent faults.

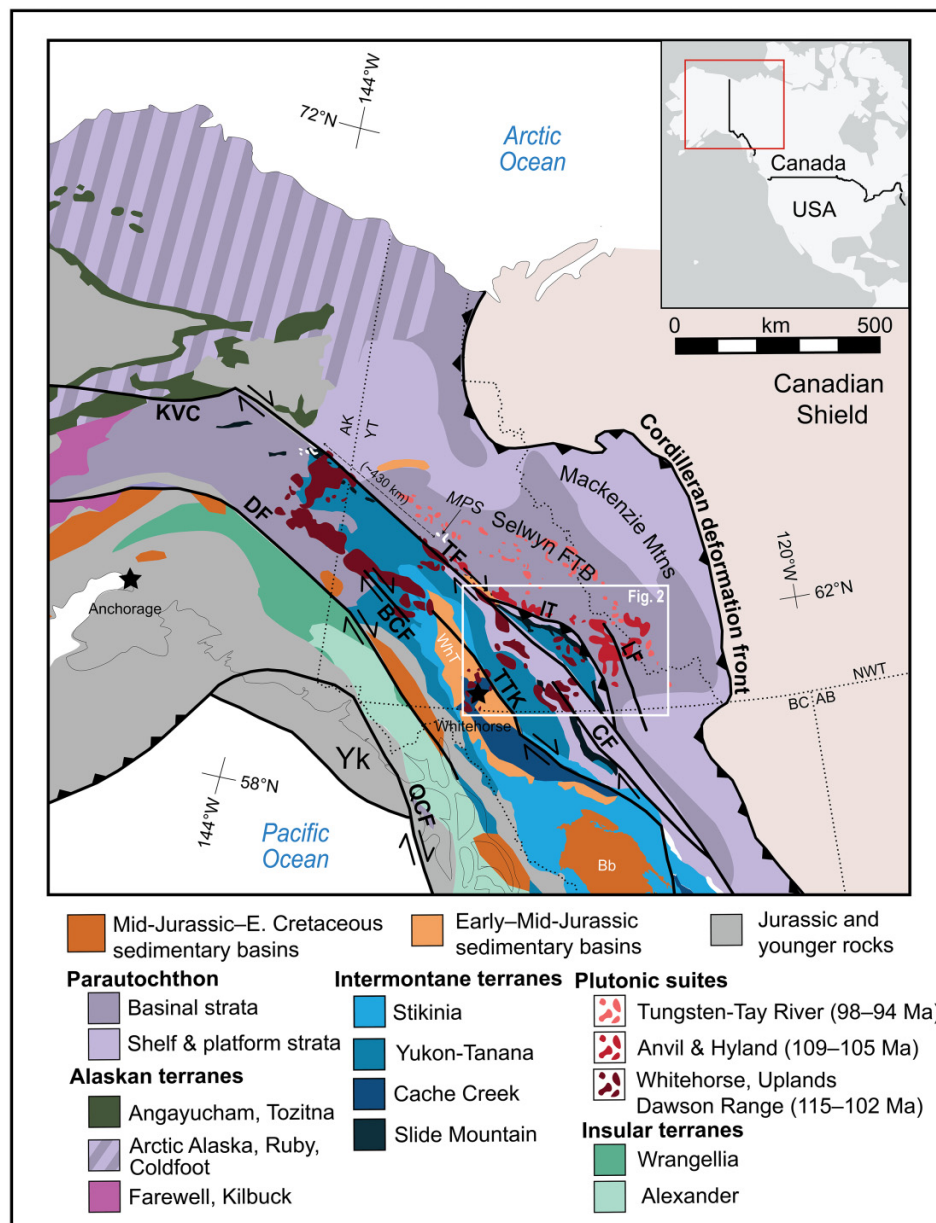
Low-temperature thermochronology data reveal the cooling and exhumation histories of rocks and can therefore be used to constrain the timing, kinematics, and magnitudes of rock exhumation through faulting by comparing the cooling histories on opposing walls of a fault system (e.g., Fraser et al. 2021; Damant et al. 2023). Here, we use multi-method low-temperature thermochronology to reveal the thermal histories of rocks in different structural positions in the Upper Hyland River Valley area (Fig. 3). We present new apatite and zircon (U-Th)/He (AHe and ZHe) and apatite fission-track (AFT) ages from 30 samples across the Logan Mountains. We use these data and thermal history modeling to infer the timing and style of slip on faults in the area. Our results highlight how fault stepovers and restraining bends associated with regional strike-slip faults can drive localized exhumation in the Northern Canadian Cordillera.

## 2. Background

### 2.1. Northern Canadian Cordillera

The Northern Canadian Cordillera has formed and evolved over >750 Myr through phases of rifting, passive margin development, and terrane accretion (e.g., Nelson et al. 2013; Monger and Gibson 2019). Siliciclastic and carbonate strata were deposited along the western passive margin of Laurentia during the Neoproterozoic to Devonian, forming the Selwyn basin (Figs. 1 and 2; Abbott et al. 1986; Gordey and

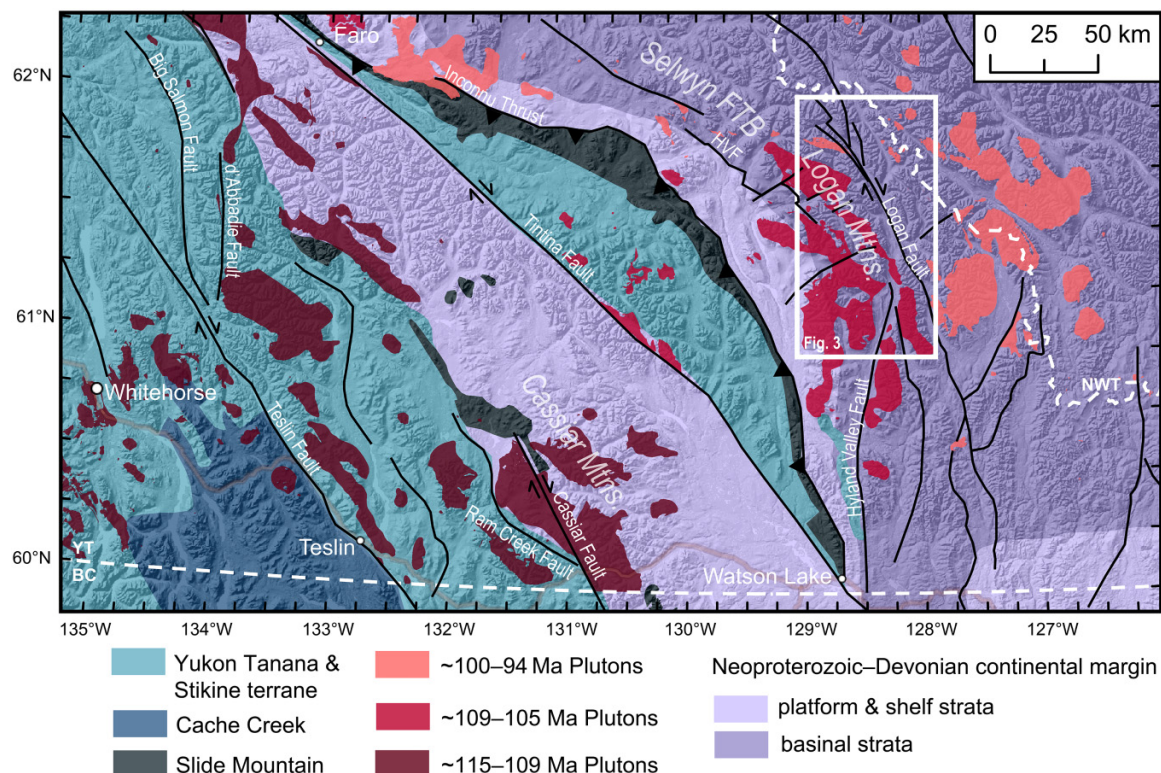
**Fig. 1.** Tectonic overview map of the Northern Cordillera. Map highlights the main faults, sedimentary basins, and terranes. Main Cretaceous plutonic suites in Yukon and Alaska from Hart et al. (2004). The apparent offset of McQuesten Suite plutons by ~430 km is shown by the dashed line with arrowheads. The white box shows the location of Fig. 2. AB—Alberta, AK—Alaska, Bb—Bowser basin, BC—British Columbia, BCF—Big Creek Fault, DF—Denali fault, FTB—Fold-Thrust Belt, IT—Inconnu thrust, KVC—Kaltag–Victoria Creek fault, LF—Logan fault, MPS—McQuesten Plutonic Suite, NWT—Northwest Territories, QCF—Queen Charlotte–Fairweather fault, TTK—Teslin–Thibert–Kutcho fault, WhT—Whitehorse Trough, Yk—Yukatut plate, YT—Yukon Territory. Modified after Colpron et al. (2015).



Anderson 1993). Eastward subduction and back-arc rifting from the Devonian–Mississippian removed a fragment of the continental margin from Laurentia. A series of Mississippian–Permian magmatic arcs formed upon this rifted fragment (Yukon–Tanana terrane), which was separated from ancestral North America by the Slide Mountain ocean (Nelson et al. 2006). Closure of the Slide Mountain ocean during the Permian was followed by arc magmatism in the Stikine and Quesnel terranes, and by final accretion of the Intermontane terranes to the North American margin by the Juras-

sic (Gabrielse 1991; Evenchick et al. 2007; Nelson and Colpron 2007; Beranek and Mortensen 2011; Monger and Gibson 2019; Colpron et al. 2022; Nelson et al. 2022). Terrane accretion resulted in thrust faulting and crustal thickening during the Jurassic and Cretaceous throughout large parts of the Northern Canadian Cordillera (e.g., Mair et al. 2006; Staples et al. 2016; Clark 2017; Gaidies et al. 2020). For example, the Jurassic Inconnu thrust places rocks of Yukon–Tanana and Slide Mountain affinities over autochthonous continental margin rocks (Fig. 2; Murphy et al. 2006). The Macken-

**Fig. 2.** Simplified geologic map of southeastern Yukon. The white box shows the location of the Upper Hyland Valley area in the Logan Mountains. Geology from the Yukon Geological Survey Bedrock Geology Dataset. Faults from the Yukon Geological Survey, Northwest Territories Geological Survey, and the British Columbia Geological Survey. FTB—fold-thrust Belt, HVF—Hyland Valley fault. The map projection is NAD 83 UTM Zone 9N.



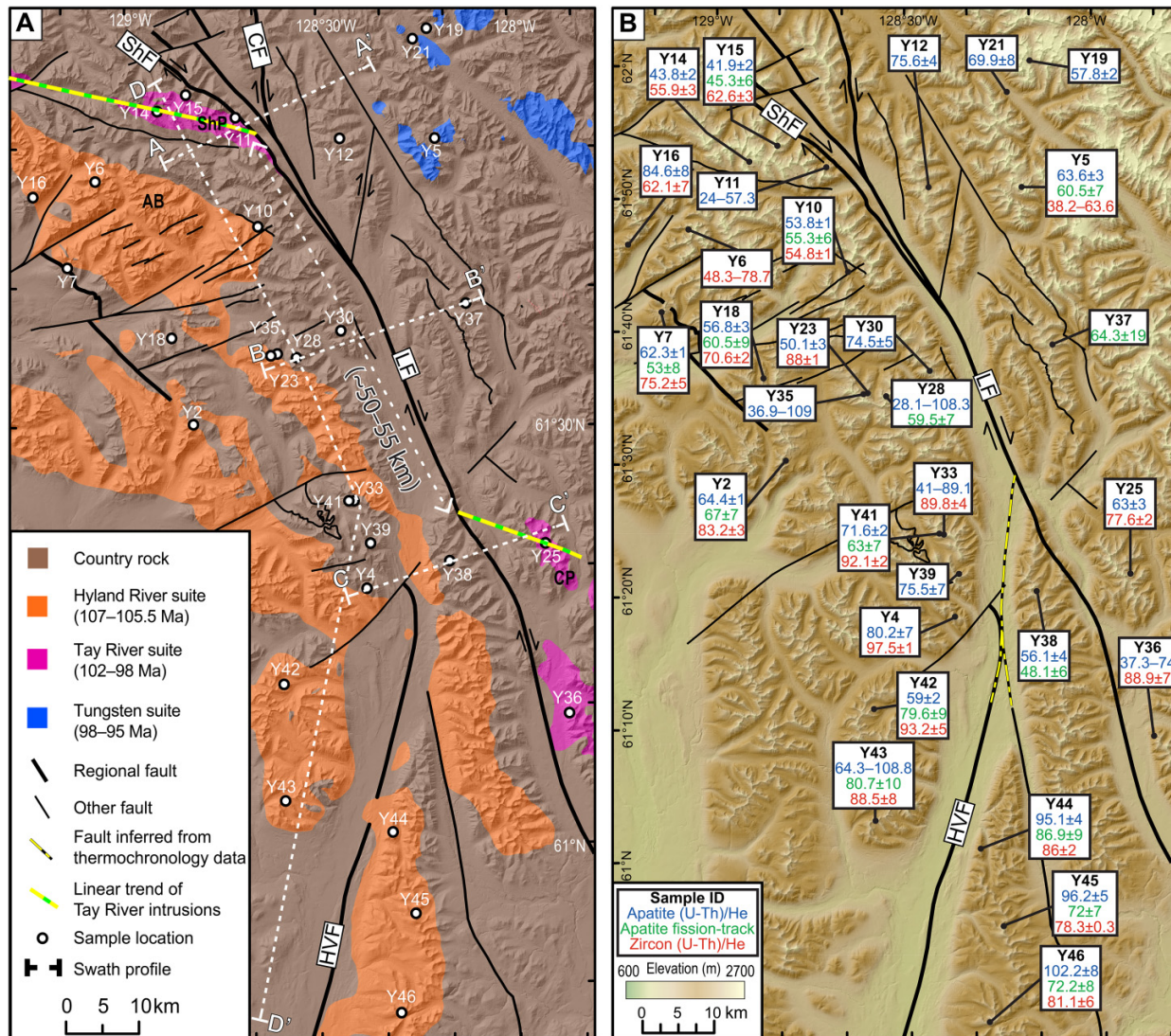
zie Mountain fold-thrust belt formed in the foreland region from the Cretaceous to early Paleocene (e.g., Powell et al. 2016).

The Cretaceous was also a time of widespread felsic-intermediate plutonism, with intrusion ages generally decreasing from southwest to northeast (Fig. 1; e.g., Hart et al. 2004; Mair et al. 2006; Rasmussen 2013). Early Cretaceous arc magmatism formed the Whitehorse and Dawson Range suites (ca. 115–102 Ma; Fig. 1; Mortensen et al. 2000). Plutons of the Anvil and Hyland suites are slightly younger and are inferred to have formed in a back-arc setting (ca. 109–105 Ma; Fig. 1; e.g., Hart et al. 2004; Rasmussen 2013). Inboard parts of the mid-Cretaceous magmatic belt include calc-alkaline rocks of the Tay River (102–98 Ma), Tungsten (98–95 Ma), Mayo (98–93 Ma), and Tombstone (94–90 Ma) plutonic suites (Fig. 1; Hart et al. 2004; Rasmussen 2013). The petrogenesis and emplacement of these plutons is debated but suggested to have involved the melting of thickened crust (e.g., Driver et al. 2000; Mair et al. 2006; Rasmussen 2013) and strike-slip faulting (Murphy et al. 1995; Gabrielse et al. 2006).

The Paleocene–Eocene was a transition period from predominately northeastward-directed compression to transpression. Dextral displacement of terranes within the Northern Canadian Cordillera occurred along a widely distributed network of northwest–southeast-striking faults (see reviews in Gabrielse et al. 2006; Monger and Gibson 2019). The Tintina fault, a lithospheric-scale structure, accommodated ~430 km

of dextral displacement during this time, based on the offset of geological markers, including the ca. 67 Ma McQuesten suite plutons (MPS in Fig. 1; Murphy et al. 1995; Murphy 1997; Murphy and Mortensen 2003; Gabrielse et al. 2006; Monger and Gibson 2019; Estève et al. 2020; Busby et al. 2023). Shearing along the western part of the ca. 100 Ma Cassiar batholith suggests that the Cassiar fault, and other strike-slip faults in the Cassiar Mountains, were active during the mid-Cretaceous, accommodating up to 100 km of dextral offset (Gabrielse 1985; Driver et al. 2000). The Teslin-Thibert-Kutcho fault system extends over ~1000 km from the Yukon into central British Columbia (Fig. 1). Estimates for this fault system suggest 130–175 km of combined displacement prior to the Late Cretaceous (Gabrielse 1985; Gabrielse et al. 2006). The Big Creek fault extends ~150 km and experienced multiple phases of slip, including during the Cretaceous and the late Paleocene–Eocene (Mottram et al. 2020, 2024). During this time, thrusting continued in the Bowser basin (Evenchick et al. 2007), reflecting the distributed nature of transpressional deformation. Farther west and outboard of the Intermontane terranes, accretion of the Insular terranes, which likely began during the Middle to Late Jurassic, continued through the Cretaceous (e.g., Vice et al. 2020). Flat-slab subduction of the Yakutat terrane underneath southern Alaska began ca. 36 Ma (Finzel et al. 2011), and oblique collision continues to the present day in southwest Yukon and southeast Alaska (e.g., Hyndman et al. 2005).

**Fig. 3.** (A) Simplified geologic map of the Upper Hyland Valley area in the Logan Mountains. The locations of swath profiles are shown in dashed white lines. The dashed brown line shows the ~50–55 km of offset of Tay River suite plutons by the Logan fault. Geology from Yukon Geological Survey Bedrock Geology Dataset, Moynihan (2016), Moynihan (2017), and field mapping by DPM. (B) Topographic map with major faults showing samples ages or age ranges in Ma. The location of (A) and (B) is shown in the white box in Fig. 2. HVF—Hyland Valley fault, LF—Logan fault, CF—Connector fault, and ShF—Shannon fault. AB—Anderson batholith, CP—Caesar pluton, ShP—Shannon pluton. The map projection (A) and (B) is NAD 83 UTM Zone 9N.



## 2.2. The Upper Hyland River Valley area

The Upper Hyland River drains the eastern part of the Logan Mountains. The area is mostly underlain by Neoproterozoic–Cambrian clastic and lesser carbonate metasedimentary rocks of the Hyland Group (Fig. 2; Gordey and Anderson 1993; Moynihan 2016). Mesozoic penetrative deformation produced southwest-vergent recumbent folds that can be traced for tens of kilometers, have amplitudes of kilometers, and account for multiple tight-isoclinal repetitions of Hyland Group stratigraphy. Intersection and stretching lineations that formed during the dominant phase of Mesozoic deformation typically plunge at shallow angles to the northwest or southeast. Rocks in the area were affected by greenschist to upper amphibolite facies regional

metamorphism (e.g., Roots et al. 1966; Moynihan 2013). The highest grade rocks are located in an elliptical region (>80 km by 30 km), centered on the northern end of the Tyers batholith (Roots et al. 1966).

Three Cretaceous magmatic suites are represented in the study area (Hart et al. 2004; Heffernan 2004; Rasmussen 2013). The Hyland River suite forms large batholiths and numerous sills and dikes in regions of high metamorphic grade. It mostly comprises weakly to undeformed, equigranular to mildly porphyritic biotite granite and granodiorite, but also includes minor biotite–hornblende diorite. Zircon U-Pb dates from the suite are in the range 106–101 Ma (Heffernan 2004). The Tay River suite includes the Shannon pluton (Figs. 3A and 4) and other smaller plutons, as well as abundant sills

and dikes (centimeter–meter wide; Rasmussen 2013). Most intrusions range from granodiorite to gabbroic diorite, but the eastern (deformed) part of the Shannon pluton includes biotite granite (Moynihan 2016). Narrow (centimeter–meter scale) dikes are porphyritic–equigranular, dacite–andesite, and typically contain hornblende and biotite. Zircon U–Pb dates from the Tay River suite range 99–95 Ma (Heffernan 2004; Rasmussen 2013). The Tungsten suite (97–94 Ma; Hart et al. 2004) is represented by small plutons in the eastern part of the area. It includes leucocratic biotite granite, monzogranite, and quartz monzonite. Cordierite- and andalusite-bearing contact metamorphic aureoles (tens to hundreds of meters wide) around intrusions of the Hyland, Tay River, and Tungsten suites suggest that plutons were emplaced at 3–3.5 kbar, equivalent to a depth of ~9–12 km (e.g., Gordey and Anderson 1993; Pattison and Vogl 2005; Moynihan 2013).

Fold structures and metamorphic isograds are truncated by batholiths of the Hyland River suite. The only mid-Cretaceous intrusions that have undergone significant penetrative deformation are early phases of the Hyland River suite and the eastern part of the Shannon pluton (Tay River suite).

The study area is transected by a regional dextral strike-slip fault system, which includes the Logan, Shannon, and Connector faults (Fig. 3A). The north–northwest-striking Logan fault can be traced across the area with a mapped (minimum) strike length of ~120 km (Fig. 3; Moynihan 2016, 2017). The Shannon fault, which is oriented slightly counterclockwise of the Logan fault, intersects the Logan fault in the Hyland River valley. This fault has a mapped strike length of ~40 km. The Connector fault extends north from the Logan fault (Fig. 3A).

The cumulative offset across the faults is poorly constrained, but large displacement is suggested by the absence of Tay River intrusions east of the Shannon fault. The Shannon pluton forms part of an approximately east–west-trending linear belt of Tay River suite intrusions north of the Anderson batholith (Fig. 3A). This trend ends abruptly at the Shannon fault, as intrusions of this suite are absent from east of the Shannon and Logan faults at this latitude. The closest pluton from the Tay River suite east of the Logan fault is the Caesar pluton, which is compositionally and mineralogically similar to parts of the Shannon pluton but is located ~65 km to the south–southeast (Fig. 3A). The Caesar pluton is interpreted to have formed along the same trend as the Shannon pluton, and their separation is attributed to dextral strike-slip faulting. This relationship suggests cumulative offset of 50–55 km of the Tay River suite plutons along the Logan and Shannon faults since their emplacement in the mid-Cretaceous (Fig. 3A).

The Shannon pluton is truncated on its east side by the Shannon fault. A narrow tail extends parallel to the fault and a penetrative foliation is developed within ~5 km of the Shannon fault (Fig. 4). The intensity of this foliation increases towards the fault, and there is an increasing prevalence of dextral kinematic indicators such as shear bands and S–C fabrics (Figs. 4C and 4D). The foliation in this penetratively deformed zone generally dips steeply ( $70^\circ$ – $90^\circ$ ) towards the southwest, whereas slip and elongation lineations are gently plunging. The Shannon fault plane dips steeply towards

the northeast; it is locally marked by several meters of heavily fractured, white weathering quartz-rich mylonite (Fig. 4B). Moynihan (2016, 2017) and Tollefson et al. (2023) interpreted temporal overlap between emplacement of the easternmost parts of the Shannon pluton and initial displacement along the Shannon fault.

### 3. Methods

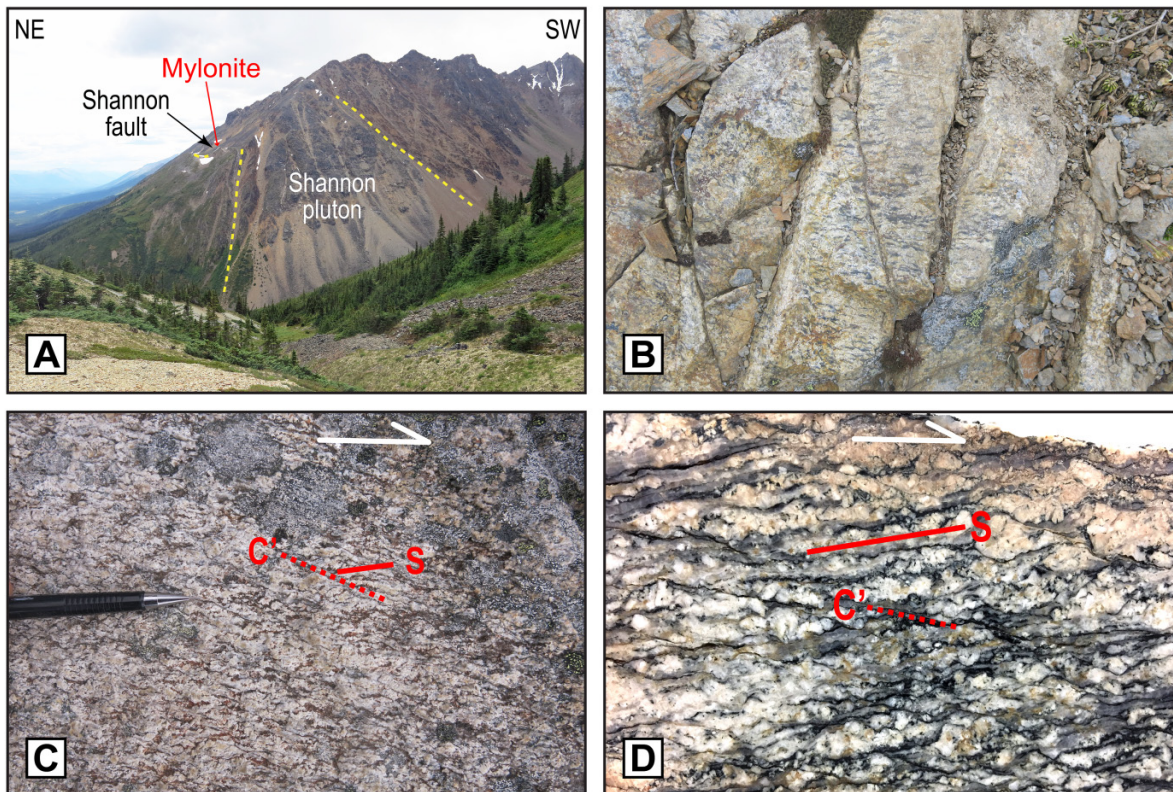
To constrain the timing and magnitude of rock cooling through the upper crust, we obtained AHe, AFT, and ZHe data. (U-Th)/He thermochronology is based on the production of  ${}^4\text{He}$  via alpha decay of  ${}^{238}\text{U}$ ,  ${}^{235}\text{U}$ ,  ${}^{232}\text{Th}$ , and  ${}^{147}\text{Sm}$ , and its temperature-dependent retention in mineral grains (e.g., Harrison and Zeitler 2005). The temperature sensitivity window for AHe and ZHe is ~70–40 °C and ~200–140 °C, respectively (e.g., Zeitler et al. 1987; Reiners et al. 2004), though in geological situations involving long residence time in the upper crust and (or) high parent nuclide content, together producing significant damage to the crystal lattice,  ${}^4\text{He}$  may be lost at much lower temperatures (e.g., Guenthner 2021; Whipp et al. 2022). Fission track thermochronology is based on the temperature-sensitive retention of fission tracks, linear damage zones produced by the spontaneous fission of  ${}^{238}\text{U}$  atoms, within a mineral's crystal lattice (e.g., Price and Walker 1963). The temperature sensitivity window for fission tracks to accumulate and partially anneal in apatite is ~120–60 °C (e.g., Laslett et al. 1987). Hence, our data together trace the thermal history of a rock through ~200–40 °C, representing ~8–1.5 km crustal depths, depending on the geothermal gradient.

We analyzed samples collected from Cretaceous igneous intrusions to maximize apatite and zircon yields and quality (Fig. 3 and Table S1). Mineral separation was undertaken at the University of Calgary and Boise State University following standard separation procedures. This included crushing and sieving, followed by density and magnetic separation techniques. All dating was conducted at the Calgary Geo- and Thermochronology Lab at the University of Calgary.

For (U-Th)/He dating, we aimed to analyze five apatite and three zircon grains per sample (Tables 1 and 2). Between 3–8 clear, inclusion-free, euhedral grains >~60  $\mu\text{m}$  in diameter were selected for dating using a Zeiss stereomicroscope. Single-grain aliquots were prepared by packing individual crystals in niobium tubes for analysis following the procedure described in McKay et al. (2021).

For AFT dating, we used the external detector method with zeta-calibration (Hurford and Green 1983) and followed the analytical procedure described in Fraser et al. (2021). Sample mounts were irradiated with thermalized neutrons at the BR1 reactor in Mol, Belgium. Fission-track analysis was done using a Zeiss AxioImager.M2m microscope with an Autoscan System stage. The zeta factor of  $263.9 \pm 22.6$  year  $\text{cm}^2$  (JP) was determined by analyzing 13 age standards (Durango and Fish Canyon Tuff) between two irradiations. We aimed to count 25–30 grains per sample and measured the diameter of four c-axis-parallel etch pits ( $D_{\text{par}}$ ) per grain as a proxy for apatite chemical composition (Donelick et al. 1999). We also

**Fig. 4.** (A) The narrow tail of the Shannon pluton viewed towards the southeast along the trend of the Hyland River valley. The Shannon fault marks the northeastern boundary of the pluton where it juxtaposed biotite granite against low-grade rocks of the Hyland Group. Relief between the lowest point visible along the fault trace and high point in the top right hand corner is approximately 800 m. A white-weathering band along the fault is composed of heavily fractured quartz-rich mylonite. (B) Fractured rocks exposed along the narrow tail of the Shannon pluton. (C) Field photograph and (D) cut slab showing asymmetric shear band fabric developed in biotite granite in the eastern part of the Shannon pluton. The white arrow in (C) and (D) shows the interpreted sense of shear. The width of (D) is approximately 7 cm. Photos taken by DPM.



measured confined track lengths and crystal c-axis orientations for our samples using TrackWorks software.

## 4. Results

### 4.1. Apatite and zircon (U-Th)/He results

We present 121 new single-grain AHe dates from 28 samples that range 110–24 Ma ([Table 1](#)). In general, our single-grain dates reproduce well in each sample. Mean ages were calculated for samples with single-grain date standard deviations <20%. Using this threshold, 22 mean AHe ages range from  $102 \pm 8$  to  $42 \pm 2$  Ma ([Fig. 3B](#); [Table 1](#)). Six samples show dispersion, and so we report the range of single-grain dates for these samples ([Fig. 3B](#); [Table 1](#)).

We present 60 new single-grain ZHe dates from 20 samples that range 102–38 Ma and report 18 mean ZHe ages that range from  $98 \pm 1$  to  $55 \pm 1$  Ma ([Fig. 3B](#); [Table 2](#)). Two samples showed dispersion, and so we report the range of single-grain dates for these samples ([Fig. 3B](#); [Table 2](#)).

Dispersion in (U-Th)/He single-grain data can be caused by a multitude of factors, including variable amounts of radiation damage, variations in grain size, parent nuclide zonation, grain fragmentation and abrasion, helium implantation, and

the presence of uranium-rich inclusions (e.g., [Flowers et al. 2022a, 2022b](#)). We plotted our single-grain dates against effective spherical radius to investigate the influence of grain size ([Figs. S1 and S2](#)). In general, our samples do not show clear trends between date and grain size, except single-grain AHe dates for samples Y4 and Y35, which exhibit negative trends with grain size. We plotted daughter versus parent isotopes (D-P plots; [Figs. S3 and S4](#); [Härtel et al. 2022](#); [Härtel and Enkelmann 2024](#)) to identify any outliers or multiple age components. Due to the small number of single-grain dates per sample (usually  $\leq 5$ ), we follow the recommendation of [Härtel and Enkelmann \(2024\)](#) and refrain from identifying trends based on a linear regression of these data. However, we do note that apparent outliers for AHe samples Y5, Y7, and Y41 show elevated amounts of daughter (i.e., alpha-corrected helium; [Fig. S3](#)). Complete single-grain AHe and ZHe datasets are available in [Tables S2 and S3](#).

### 4.2. Apatite fission-track results

We present 15 new AFT ages ([Fig. 3B](#); [Table 3](#)). We applied the  $\chi^2$  test to assess the likelihood that single-grain dates represent a single-age population. All samples passed the  $\chi^2$  test ( $\chi^2 > 5\%$ ) and pooled ages range from  $87 \pm 9$  to

**Table 1.** Summary of single-grain apatite (U-Th)/He results from the Upper Hyland River Valley, Yukon.

Sample ID	<sup>4</sup> He (fmol/ $\mu$ g)	U (ppm)	Th (ppm)	eU (ppm)	R <sub>s</sub> ( $\mu$ m)	Uncorrected date (Ma)	Ft	Corrected date (Ma)	2 $\sigma$
Y2-1	8.44	24.67	37.54	36.61	49.2	46.12	0.707	65.2	1.2
Y2-2	8.27	21.95	42.53	35.13	58.0	47.30	0.755	62.6	1.2
Y2-3	7.95	19.26	42.61	32.37	59.7	49.51	0.757	65.4	1.3
Y2-4	7.05	20.12	30.36	29.71	55.0	47.37	0.738	64.2	1.2
							<b>Mean age</b>	<b>64.4</b>	<b>0.6</b>
Y4-1	4.44	7.43	28.60	14.40	55.4	57.16	0.743	76.9	2.1
Y4-2	13.66	24.17	75.82	42.68	37.1	59.26	0.629	94.2	2.4
Y4-4	4.48	8.63	26.62	15.12	69.0	54.81	0.791	69.3	2.3
							<b>Mean age</b>	<b>80.2</b>	<b>7.3</b>
Y5-1	14.69	53.75	30.58	65.82	37.5	44.31	0.643	68.9	1.4
Y5-2	11.54	40.03	29.89	51.59	46.4	44.94	0.706	63.7	1.4
Y5-3	10.17	32.01	28.57	43.22	47.1	47.96	0.728	65.9	1.5
Y5-4	13.93	27.53	31.94	40.43	43.5	72.00	0.727	99.0	2.8
Y5-5	11.22	39.75	40.65	54.03	55.1	41.70	0.747	55.8	1.1
							<b>Mean age</b>	<b>63.6</b>	<b>2.8</b>
Y7-1	3.74	11.83	24.02	18.51	39.2	39.37	0.629	62.6	1.2
Y7-2	50.05	117.20	95.73	142.00	36.9	66.30	0.623	106.4	2.0
Y7-3	0.52	2.56	0.29	2.68	35.9	36.61	0.611	59.9	3.6
Y7-4	5.99	17.73	43.74	29.70	41.5	39.27	0.647	60.7	1.5
Y7-5	7.62	27.24	31.59	36.07	35.5	40.61	0.614	66.1	2.0
							<b>Mean age</b>	<b>62.3</b>	<b>1.4</b>
Y10-1	0.78	3.01	2.96	5.08	44.1	37.02	0.675	54.8	5.0
Y10-2	2.85	11.55	0.97	13.72	46.6	43.89	0.701	62.6	2.7
Y10-3	1.59	7.39	0.25	8.48	48.5	38.99	0.711	54.8	2.6
Y10-4	3.19	12.46	5.64	15.96	60.1	42.09	0.786	53.5	1.2
Y10-5	1.76	5.89	9.34	10.30	56.8	38.79	0.745	52.1	1.9
							<b>Mean age</b>	<b>53.8</b>	<b>0.7</b>
Y11-1	0.65	0.81	22.66	6.44	71.2	18.81	0.784	24.0	0.9
Y11-2	0.30	0.47	5.15	1.90	94.3	29.06	0.837	34.7	1.1
Y11-3	2.73	4.93	25.52	11.46	63.8	44.15	0.770	57.3	1.7
							<b>Age range</b>	<b>24.0–57.3</b>	
Y12-1	3.85	7.01	30.68	15.11	35.0	49.61	0.573	86.6	2.5
Y12-2	4.19	7.06	29.68	15.21	42.6	54.57	0.684	79.8	1.9
Y12-3	3.26	7.59	30.63	15.73	38.9	40.43	0.623	64.9	1.1
Y12-4	4.25	8.01	36.77	17.68	37.6	46.74	0.600	77.9	2.1
Y12-5	4.31	10.15	41.54	21.18	35.2	39.68	0.578	68.6	1.5
							<b>Mean age</b>	<b>75.6</b>	<b>3.9</b>
Y14-1	5.27	18.20	38.53	30.49	50.7	35.24	0.726	48.5	1.1
Y14-2	4.61	18.10	35.26	29.52	40.5	31.87	0.677	47.1	1.5
Y14-3	4.84	20.07	41.98	33.22	40.2	29.54	0.669	44.2	1.1
Y14-4	3.99	18.42	33.62	29.90	40.4	27.58	0.698	39.5	1.0
Y14-5	5.50	26.03	49.33	41.67	39.0	26.71	0.676	39.5	0.9
							<b>Mean age</b>	<b>43.8</b>	<b>1.9</b>
Y15-1	2.43	7.36	25.61	14.71	49.5	33.09	0.713	46.4	1.2
Y15-2	2.18	9.19	26.43	16.71	50.6	25.86	0.723	35.8	0.9
Y15-3	2.20	8.53	30.35	17.35	42.9	25.62	0.668	38.4	0.7
Y15-4	2.77	9.62	32.16	18.96	44.7	29.44	0.678	43.4	1.2
Y15-5	3.00	9.35	38.81	20.36	40.0	29.61	0.649	45.6	1.5
							<b>Mean age</b>	<b>41.9</b>	<b>2.1</b>
Y16-1	17.86	56.17	9.59	60.65	35.2	56.51	0.602	93.9	2.5
Y16-2	10.98	35.84	2.40	38.03	51.3	55.74	0.726	76.8	1.8
Y16-3	13.14	30.83	18.31	36.70	43.0	68.94	0.677	101.8	2.3

**Table 1.** (continued).

Sample ID	${}^4\text{He}$ (fmol/ $\mu\text{g}$ )	U (ppm)	Th (ppm)	eU (ppm)	$R_s$ ( $\mu\text{m}$ )	Uncorrected date (Ma)	Ft	Corrected date (Ma)	$2\sigma$
Y16-4	16.42	60.58	8.14	64.20	53.9	48.71	0.739	65.9	1.0
							<b>Mean age</b>	<b>84.6</b>	<b>8.1</b>
Y18-1	4.62	22.32	18.59	28.23	37.1	31.89	0.673	47.4	1.8
Y18-2	2.51	8.20	13.61	12.70	40.3	40.19	0.704	57.1	2.0
Y18-3	1.60	4.58	9.66	7.87	44.7	42.46	0.757	56.1	2.2
Y18-4	3.06	8.89	8.24	11.94	50.2	51.60	0.761	67.8	2.1
Y18-5	2.47	7.39	10.37	10.77	67.6	46.00	0.825	55.8	1.1
							<b>Mean age</b>	<b>56.8</b>	<b>3.3</b>
Y19-1	20.01	36.31	45.93	51.84	73.8	44.05	0.751	58.7	1.3
Y19-2	11.54	48.64	34.41	61.97	50.0	43.11	0.741	58.2	1.2
Y19-3	10.90	38.87	27.58	49.62	55.4	48.36	0.768	63.0	1.7
Y19-4	6.49	22.84	19.70	30.80	52.5	77.50	0.807	96.0	1.5
Y19-5	7.77	24.41	21.07	32.57	59.2	37.33	0.725	51.5	1.1
							<b>Mean age</b>	<b>57.8</b>	<b>2.4</b>
Y21-2	6.99	27.30	12.17	32.73	38.1	42.56	0.657	64.8	1.4
Y21-3	9.78	30.12	8.43	34.21	38.1	56.09	0.659	85.1	1.9
Y21-5	13.33	56.76	11.27	62.44	43.4	41.46	0.694	59.7	1.0
							<b>Mean age</b>	<b>69.9</b>	<b>7.8</b>
Y23-1	5.92	20.76	26.14	27.18	68.5	40.31	0.832	48.5	1.3
Y23-2	8.53	28.77	28.65	35.85	55.0	44.04	0.751	58.6	1.8
Y23-3	5.09	18.75	22.33	24.29	73.8	38.82	0.846	45.9	1.8
Y23-4	8.34	17.90	29.09	24.99	75.5	61.70	0.847	72.8	1.8
Y23-5	2.36	9.31	6.41	10.93	69.6	39.88	0.839	47.5	1.7
							<b>Mean age</b>	<b>50.1</b>	<b>2.9</b>
Y25-1	21.63	60.32	217.76	113.45	32.1	35.36	0.575	61.5	2.7
Y25-2	32.79	78.16	279.95	146.53	37.4	41.47	0.628	66.0	2.1
Y25-3	36.94	72.15	272.67	138.58	44.3	49.38	0.680	72.6	1.7
Y25-4	7.05	17.23	63.84	32.77	49.6	39.87	0.710	56.2	1.5
Y25-5	29.60	96.77	264.63	161.48	32.2	33.98	0.580	58.6	1.5
							<b>Mean age</b>	<b>63.0</b>	<b>2.9</b>
Y28-2	0.11	0.95	0.07	1.03	46.4	21.54	0.708	30.4	1.7
Y28-3	6.04	20.71	23.62	27.88	52.2	42.36	0.737	57.5	1.7
Y28-4	9.17	77.07	49.41	91.87	42.2	19.15	0.682	28.1	0.6
Y28-5	5.81	24.11	14.46	29.19	46.5	38.94	0.710	54.8	1.3
Y28-7	14.73	22.32	54.05	35.45	47.9	76.79	0.709	108.3	3.4
							<b>Age range</b>	<b>28.1–108.3</b>	
Y30-1	7.77	20.28	4.72	21.57	63.0	66.48	0.806	82.5	3.1
Y30-2	5.30	18.30	0.12	18.49	43.5	52.96	0.698	75.9	3.3
Y30-3	2.75	6.46	-0.04	6.57	44.8	77.07	0.736	104.7	5.9
Y30-4	10.54	34.10	15.24	37.90	58.5	51.38	0.787	65.3	2.2
							<b>Mean age</b>	<b>74.5</b>	<b>5.0</b>
Y33-1	2.26	3.46	17.62	7.75	56.9	54.01	0.744	72.6	1.8
Y33-2	3.37	13.60	22.69	19.20	68.8	32.52	0.794	41.0	0.9
Y33-3	8.14	12.05	40.05	21.85	71.9	68.94	0.798	86.4	1.8
Y33-4	2.80	3.97	15.56	7.79	57.5	66.62	0.748	89.1	2.8
Y33-5	4.82	6.28	88.62	27.51	66.8	32.52	0.770	42.2	0.9
							<b>Age range</b>	<b>41.0–89.1</b>	
Y35-1	1.47	8.29	4.02	9.31	66.2	29.18	0.791	36.9	1.3
Y35-2	1.71	2.28	7.34	4.07	49.6	77.90	0.715	109.0	4.8
Y35-3	0.10	0.34	0.05	0.36	131.2	53.33	0.891	59.9	4.1
Y35-4	5.66	15.33	0.44	15.56	90.0	67.15	0.848	79.2	2.5
							<b>Age range</b>	<b>36.9–109.0</b>	
Y36-1	5.59	14.70	73.77	32.64	47.3	31.78	0.690	46.1	1.2
Y36-2	4.50	14.36	64.27	30.10	57.9	27.76	0.744	37.3	0.8

**Table 1.** (concluded).

Sample ID	${}^4\text{He}$ (fmol/ $\mu\text{g}$ )	U (ppm)	Th (ppm)	eU (ppm)	$R_s$ ( $\mu\text{m}$ )	Uncorrected date (Ma)	Ft	Corrected date (Ma)	$2\sigma$					
Y36-3	10.38	27.53	67.60	44.09	58.4	43.59	0.786	55.5	1.1					
Y36-4	3.92	6.64	27.02	13.24	55.4	54.79	0.740	74.0	2.4					
Y36-5	6.24	10.75	59.89	25.30	47.5	45.69	0.723	63.2	2.0					
						<b>Age range</b> <b>37.3–74.0</b>								
Y38-1	4.30	8.90	29.87	18.32	53.4	48.87	0.732	66.8	0.0					
Y38-2	2.97	7.58	26.39	15.76	56.0	39.01	0.738	52.9	0.0					
Y38-3	3.75	9.57	30.80	19.37	57.8	40.37	0.751	53.8	0.0					
Y38-5	3.42	8.69	28.44	17.22	69.4	40.43	0.790	51.2	0.0					
						<b>Mean age</b> <b>56.1</b> <b>3.6</b>								
Y39-1	7.12	18.60	2.08	19.36	62.1	67.87	0.783	86.7	2.0					
Y39-3	6.93	20.65	1.70	21.29	56.9	60.12	0.764	78.7	3.7					
Y39-4	7.98	22.31	1.37	22.87	63.1	64.42	0.786	82.0	2.2					
Y39-5	5.29	13.18	33.38	21.52	86.6	45.50	0.832	54.7	1.1					
						<b>Mean age</b> <b>75.5</b> <b>7.1</b>								
Y41-1	4.26	8.12	21.52	13.50	66.9	58.32	0.786	74.2	1.7					
Y41-2	3.89	7.39	20.73	12.59	67.7	57.16	0.787	72.6	1.7					
Y41-3	9.60	13.48	42.33	23.93	61.2	74.17	0.765	97.0	2.6					
Y41-4	4.92	9.13	23.41	15.01	89.2	60.59	0.837	72.4	1.7					
Y41-5	5.36	12.62	28.29	19.74	55.7	50.24	0.747	67.3	1.8					
						<b>Mean age</b> <b>71.6</b> <b>1.5</b>								
Y42-1	6.81	21.15	65.67	37.17	33.5	33.94	0.580	58.5	2.5					
Y42-2	7.77	18.30	58.59	32.54	43.8	44.24	0.672	65.8	3.0					
Y42-3	7.52	19.77	60.09	34.42	43.2	40.49	0.671	60.3	2.2					
Y42-4	5.66	17.00	50.07	29.24	40.1	35.89	0.650	55.2	2.2					
Y42-5	5.78	18.64	49.32	30.70	38.5	34.89	0.633	55.1	2.9					
						<b>Mean age</b> <b>59.0</b> <b>2.0</b>								
Y43-1	5.92	15.40	36.97	24.58	46.7	44.59	0.693	64.3	2.8					
Y43-2	15.56	22.41	67.95	39.13	43.8	73.52	0.676	108.8	4.0					
Y43-3	7.03	13.96	35.55	22.80	50.6	57.07	0.738	77.3	3.2					
Y43-4	11.49	19.15	44.47	30.14	55.0	70.50	0.740	95.3	3.5					
						<b>Age range</b> <b>64.3–108.8</b>								
Y44-1	8.81	25.07	4.64	26.42	36.9	61.60	0.664	92.8	4.5					
Y44-2	12.57	37.33	8.00	39.56	39.8	58.67	0.670	87.6	4.2					
Y44-4	15.09	35.88	7.09	37.81	44.1	73.62	0.701	105.0	5.5					
						<b>Mean age</b> <b>95.1</b> <b>4.5</b>								
Y45-1	13.62	35.38	9.34	37.89	46.9	66.36	0.731	90.8	4.3					
Y45-2	14.06	37.11	8.66	39.44	47.5	65.78	0.718	91.6	4.4					
Y45-3	16.55	34.12	16.59	38.41	55.2	79.47	0.749	106.1	4.5					
						<b>Mean age</b> <b>96.2</b> <b>5.0</b>								
Y46-1	11.30	20.98	14.95	24.81	51.9	84.01	0.764	110.0	4.9					
Y46-3	13.36	37.15	10.34	39.84	38.5	61.93	0.656	94.4	4.3					
						<b>Mean age</b> <b>102.2</b> <b>7.7</b>								

Note: Single-grain data in italics were excluded from mean age calculation.

Ft—alpha-ejection correction calculated following the method of Farley (2002).

$R_s$ —spherical radius, eU—effective uranium.

$45 \pm 6$  Ma (Fig. 3B; Table 3). We measured confined track lengths in each of our 15 samples (Table 3) and present the projected lengths to the crystallographic c-axis to account for anisotropic fission-track annealing (Fig. S4; Donelick et al. 1999). Mean projected confined track lengths range from  $11.97 \pm 0.58$  to  $14.41 \pm 1.22$   $\mu\text{m}$  (Table 3). Mean  $D_{\text{par}}$  values range from  $1.73 \pm 0.73$  to  $3.06 \pm 0.40$   $\mu\text{m}$  (Table 3). Single-

grain data and individual track length measurements are available in the supplementary material (Tables S4 and S5). C-axis projected confined track length distributions are presented in Fig. S5. D–P plots for all samples show positive linear trends indicating a single age component (Fig. S6). Radial plots are presented in Fig. S7. Complete single-grain AFT data are available in Table S4.

**Table 2.** Summary of single-grain zircon (U-Th)/He results from the Upper Hyland River Valley, Yukon.

Sample ID	<sup>4</sup> He (fmol/μg)	U (ppm)	Th (ppm)	eU (ppm)	R <sub>s</sub> (μm)	Uncorrected date (Ma)	Ft	Corrected date (Ma)	2σ
Y2-1	231.4	533.9	302.0	605.8	60.4	70.9	0.809	87.7	2.3
Y2-2	573.9	1692.5	549.4	1823.3	43	58.5	0.740	79.1	2.4
Y2-3	211.2	537.6	307.8	610.9	51.2	64.2	0.777	82.7	1.9
							<b>Mean age</b>	<b>83.2</b>	<b>2.5</b>
Y4-1	164.3	321.0	212.8	371.6	72.3	81.6	0.839	97.2	2.3
Y4-2	193.9	386.8	234.7	442.7	62.5	80.8	0.814	99.2	2.8
Y4-3	177.2	350.8	203.1	399.2	79.3	81.8	0.852	96.1	2.6
							<b>Mean age</b>	<b>97.5</b>	<b>0.9</b>
Y5-1	218.5	755.0	274.6	820.4	51.3	49.6	0.779	63.6	1.4
Y5-2	544.4	2532.1	367.1	2619.4	41.7	38.7	0.735	52.7	1.0
Y5-3	526.4	3490.9	194.2	3537.1	40.5	27.8	0.727	38.2	1.1
							<b>Age range</b>	<b>38.2–63.6</b>	
Y6-1	183.4	452.2	351.7	535.9	60.5	63.6	0.808	78.7	1.8
Y6-2	156.2	537.4	976.7	769.9	49	37.8	0.782	48.3	1.0
Y6-3	295.8	1151.3	1220.0	1441.7	38.7	38.2	0.707	54.0	1.3
							<b>Age range</b>	<b>48.3–78.7</b>	
Y7-1	492.7	1223.9	657.5	1380.4	54.2	66.3	0.789	84.1	1.9
Y7-2	685.7	1945.6	999.1	2183.4	47.2	58.4	0.778	75.1	1.4
Y7-3	476.7	1527.7	847.2	1729.4	46	51.3	0.772	66.4	1.3
							<b>Mean age</b>	<b>75.2</b>	<b>5.1</b>
Y10-1	197.4	827.0	129.9	857.9	45.2	42.9	0.752	57.0	1.1
Y10-2	300.0	1302.4	149.7	1338.1	43.5	41.8	0.780	53.5	1.3
Y10-3	267.7	1221.9	144.3	1256.2	38.7	39.7	0.738	53.8	1.4
							<b>Mean age</b>	<b>54.8</b>	<b>1.1</b>
Y14-1	127.8	478.2	259.4	540.0	62.5	44.1	0.815	54.1	1.5
Y14-2	258.7	1042.1	675.0	1202.8	47.6	40.1	0.760	52.7	0.9
Y14-3	137.3	455.8	244.6	514.0	64.8	49.7	0.815	61.0	2.2
							<b>Mean age</b>	<b>55.9</b>	<b>2.6</b>
Y15-1	86.5	303.7	171.8	344.6	45.7	46.7	0.752	62.1	1.4
Y15-2	89.5	324.8	234.5	380.6	45.3	43.8	0.749	58.4	1.3
Y15-3	120.6	371.6	245.1	429.9	53.8	52.2	0.777	67.2	1.9
							<b>Mean age</b>	<b>62.6</b>	<b>2.5</b>
Y16-1	74.1	313.9	53.3	326.5	44.3	42.3	0.735	57.5	1.1
Y16-2	133.5	417.2	107.5	442.7	43	56.1	0.740	75.8	1.4
Y16-3	179.5	840.9	90.6	862.5	41.5	38.8	0.732	53.0	1.2
							<b>Mean age</b>	<b>62.1</b>	<b>7.0</b>
Y18-1	165.7	407.7	370.7	495.9	102.7	62.1	0.902	68.8	1.1
Y18-2	109.0	255.3	207.0	304.6	91.9	66.5	0.884	75.2	1.4
Y18-3	130.5	321.6	337.6	402.0	101.4	60.3	0.892	67.7	1.2
							<b>Mean age</b>	<b>70.6</b>	<b>2.4</b>
Y23-1	1310.8	2556.8	2579.4	3170.7	81.3	76.3	0.855	89.3	5.5
Y23-2	1199.0	2406.8	2579.1	3020.7	79.4	73.3	0.852	86.0	3.6
Y23-3	1237.8	2509.1	2708.2	3153.6	64	72.5	0.818	88.6	3.4
							<b>Mean age</b>	<b>88.0</b>	<b>1.0</b>
Y25-1	184.8	521.9	298.1	592.9	50.2	57.6	0.772	74.6	3.2
Y25-2	293.5	748.6	519.1	872.1	57.3	62.2	0.798	77.9	1.6
Y25-3	201.5	488.9	470.6	600.9	51.1	62.0	0.773	80.2	2.0
							<b>Mean age</b>	<b>77.6</b>	<b>1.6</b>
Y33-1	301.5	632.9	338.7	713.5	60.2	78.0	0.808	96.5	2.5
Y33-2	497.6	1215.6	727.7	1388.8	55.4	66.2	0.793	83.4	2.7
Y33-3	190.4	408.8	238.5	465.6	74.7	75.4	0.843	89.5	2.6
							<b>Mean age</b>	<b>89.8</b>	<b>3.8</b>
Y36-1	116.7	243.5	151.0	279.4	52.6	77.1	0.783	98.4	2.3
Y36-2	155.1	440.6	189.1	485.6	51.1	59.0	0.779	75.7	3.0

**Table 2.** (concluded).

Sample ID	${}^4\text{He}$ (fmol/ $\mu\text{g}$ )	U (ppm)	Th (ppm)	eU (ppm)	$R_s$ ( $\mu\text{m}$ )	Uncorrected date (Ma)	Ft	Corrected date (Ma)	$2\sigma$
Y36-3	144.4	325.7	143.4	359.8	56.7	74.0	0.799	92.7	2.5
							<b>Mean age</b>	<b>88.9</b>	<b>6.8</b>
Y41-1	432.5	941.9	425.4	1043.1	68.7	76.5	0.832	91.9	3.2
Y41-2	279.8	615.4	303.3	687.6	77.5	75.1	0.849	88.4	3.4
Y41-3	278.7	566.2	301.7	638.0	72.3	80.5	0.839	96.0	2.9
							<b>Mean age</b>	<b>92.1</b>	<b>2.2</b>
Y42-1	298.4	736.6	606.7	881.0	41.4	62.6	0.727	86.1	2.3
Y42-2	240.0	489.1	278.5	555.4	52.3	79.7	0.782	101.9	2.6
Y42-3	415.5	904.9	840.7	1105.0	47.5	69.4	0.759	91.5	2.3
							<b>Mean age</b>	<b>93.2</b>	<b>4.7</b>
Y43-1	542.7	1492.9	1017.4	1735.1	53.2	57.8	0.784	73.7	2.3
Y43-2	271.5	527.2	242.9	585.0	69.5	85.5	0.834	102.6	2.9
Y43-3	311.3	657.3	459.5	766.6	73.4	74.9	0.841	89.1	4.2
							<b>Mean age</b>	<b>88.5</b>	<b>8.3</b>
Y44-1	360.2	1011.0	112.7	1037.8	44.2	64.1	0.748	85.6	2.0
Y44-2	185.7	460.9	71.7	478.0	58.4	71.7	0.805	89.0	2.4
Y44-4	334.7	878.8	143.2	912.9	60.6	67.7	0.812	83.3	3.8
							<b>Mean age</b>	<b>86.0</b>	<b>1.7</b>
Y45-4	341.9	1036.6	111.3	1063.1	45.5	59.4	0.754	78.8	3.5
Y45-5	206.0	565.7	143.5	599.9	59.1	63.4	0.807	78.6	3.0
Y45-6	244.9	747.5	108.9	773.4	45.3	58.5	0.753	77.6	3.1
							<b>Mean age</b>	<b>78.3</b>	<b>0.3</b>
Y46-4	177.8	567.7	65.8	583.3	53	56.3	0.789	71.4	3.5
Y46-5	301.4	912.4	82.1	931.9	43.3	59.7	0.743	80.4	3.3
Y46-6	191.8	492.7	116.1	520.3	43.4	68.0	0.743	91.5	3.0
							<b>Mean age</b>	<b>81.1</b>	<b>5.8</b>

Note: Ft—alpha-ejection correction calculated following the method of [Farley \(2002\)](#).

$R_s$ —spherical radius, eU—effective uranium.

**Table 3.** Summary of apatite fission-track results from the Upper Hyland River Valley, Yukon.

Sample	N	Ns	Ni	$\rho_s$ ( $\text{cm}^{-2}$ )	$\rho_i$ ( $\text{cm}^{-2}$ )	$\rho_d$ ( $\text{cm}^{-2}$ )	U (ppm)	$\chi^2$ (%)	Age $\pm 1\sigma$ (Ma)	$D_{\text{par}} \pm 1\sigma$ ( $\mu\text{m}$ )	Mean track length $\pm 1\sigma$ ( $\mu\text{m}$ ) (n)
Y2	29	335	714	8.07E+05	1.67E+06	1.03E+06	24.4 $\pm$ 2.1	93.6	67.0 $\pm$ 7.3	2.36 $\pm$ 0.25	14.41 $\pm$ 1.22 (50)
Y5	30	357	794	1.11E+06	2.27E+06	1.02E+06	33.3 $\pm$ 2.1	6.2	60.5 $\pm$ 6.6	2.45 $\pm$ 0.24	14.18 $\pm$ 1.24 (11)
Y7	23	108	273	4.63E+05	2.03E+06	1.02E+06	29.8 $\pm$ 2.1	86.6	53.0 $\pm$ 7.6	2.15 $\pm$ 0.44	12.23 $\pm$ 0.29 (2)
Y10	30	335	809	6.56E+05	1.41E+06	1.02E+06	20.8 $\pm$ 1.8	54.6	55.3 $\pm$ 6.1	2.05 $\pm$ 0.23	13.58 $\pm$ 1.59 (51)
Y15	29	155	455	3.44E+05	8.51E+05	1.01E+06	12.6 $\pm$ 0.6	54.8	45.4 $\pm$ 5.8	2.48 $\pm$ 0.37	13.99 $\pm$ 1.34 (23)
Y18	14	88	193	5.48E+05	1.25E+06	1.01E+06	18.6 $\pm$ 4.2	92.4	60.5 $\pm$ 9.4	2.20 $\pm$ 0.40	11.97 $\pm$ 0.58 (3)
Y28	25	206	458	9.23E+05	1.84E+06	1.01E+06	27.4 $\pm$ 2.3	77.2	59.5 $\pm$ 7.2	2.24 $\pm$ 0.23	13.68 $\pm$ 1.61 (32)
Y37	7	19	39	9.19E+04	1.99E+05	1.01E+06	3.0 $\pm$ 0.6	43.0	64.3 $\pm$ 18.9	1.99 $\pm$ 0.23	13.48 $\pm$ 2.11 (2)
Y38	25	225	616	2.61E+05	7.23E+05	1.00E+06	10.8 $\pm$ 0.7	70.8	48.1 $\pm$ 5.7	3.06 $\pm$ 0.40	14.61 $\pm$ 1.1 (35)
Y41	27	370	772	4.86E+05	9.60E+05	1.00E+06	14.4 $\pm$ 0.9	87.5	63.0 $\pm$ 6.8	2.05 $\pm$ 0.25	14.08 $\pm$ 1.35 (51)
Y42	28	252	415	6.33E+05	9.43E+05	1.00E+06	14.2 $\pm$ 1.1	74.8	79.6 $\pm$ 9.5	2.27 $\pm$ 0.14	14.26 $\pm$ 1.16 (53)
Y43	25	247	399	6.63E+05	1.06E+06	9.94E+05	16.0 $\pm$ 1.5	55.1	80.7 $\pm$ 9.7	2.13 $\pm$ 0.20	13.89 $\pm$ 1.07 (40)
Y44	25	546	816	1.41E+06	2.18E+06	9.90E+05	33.0 $\pm$ 1.8	34.6	86.9 $\pm$ 9.1	2.00 $\pm$ 0.24	14.04 $\pm$ 1.05 (99)
Y45	25	609	1096	1.65E+06	2.86E+06	9.87E+05	43.5 $\pm$ 1.8	11.2	72.0 $\pm$ 7.3	1.73 $\pm$ 0.13	13.76 $\pm$ 1.2 (75)
Y46	16	266	474	1.11E+06	1.92E+06	9.81E+05	29.4 $\pm$ 3.0	38.7	72.2 $\pm$ 8.4	1.90 $\pm$ 0.53	13.15 $\pm$ 1.81 (11)

Note: N—number of grains, Ns—spontaneous track count, Ni—induced track count,

$\rho_s$ —spontaneous track density,  $\rho_i$ —induced track density,  $\rho_d$ —dosimeter track density,

U—mean sample uranium concentration,  $\chi^2$ —chi-squared test probability (>5% passes; <5% fails),

$D_{\text{par}}$ —fission-track etch pit diameter measured parallel to the c-axis.

Mean track length is c-axis projected.

## 5. Thermal history modeling

### 5.1. Modeling approach

Inverse thermal history modeling was conducted using HeFTy v2.1.4 software (Ketcham 2005, 2024) to explore possible time-temperature (*t-T*) histories that are consistent with our measured thermochronology data and other available geologic constraints, such as crystallization ages. HeFTy uses a Monte Carlo search algorithm to identify *t-T* histories and assigns them a goodness-of-fit based on how well each thermal history reproduces the measured single-grain data and (or) fission-track confined track length distribution.

Single-grain AHe and ZHe data, fission-track single-grain data, and confined track lengths, when available, were incorporated into our thermal history models. Complete documentation of the inputs for each model is provided in the supplemental material (Table S6) following the reporting protocol of Farley (2002); Flowers et al. (2022b). We used the diffusion models of Flowers et al. (2009) and Guenthner et al. (2013) for AHe and ZHe data, respectively, and the AFT annealing model of Ketcham et al. (2007). We started with an uncertainty of 10% on single-grain (U-Th)/He dates and increased it by 10% as needed to find acceptable thermal histories (e.g., Wildman et al. 2016; Damant et al. 2023). Each model was set to generate and test 50,000 possible *t-T* paths. In HeFTy, *t-T* paths are assigned a “good” or “acceptable” fit using a goodness-of-fit value; values between 0.05 and 0.5 indicate an acceptable fit of the modeled data for a tested *t-T* path to the measured data, and greater than 0.5 represents a good fit. Paths that yielded goodness-of-fit values less than 0.05 are automatically discarded by HeFTy. We set up our modeling window to search for thermal histories beginning at 110 Ma, slightly older than the suggested emplacement age of the oldest plutons in our study area. The end of each thermal history was a final constraint of  $5 \pm 5$  °C at 0 Ma to reflect the present-day surface conditions.

We included *t-T* constraint boxes to aid the program in finding thermal histories that fit with the data and available geological constraints. An initial constraint box was included to represent the intrusion ages of the sampled plutons (Hart et al. 2004). Additional constraint boxes were set based on our thermochronology data. For samples with (U-Th)/He data, a constraint box that spanned the range of single-grain dates  $\pm 15$  Myr (i.e., 15 Myr older than the oldest single-grain date and 15 Myr younger than the youngest single-grain date) was included. The height of these boxes was dictated by the temperature sensitivity window of the AHe (70–40 °C) and ZHe (200–140 °C) thermochronometers. When AFT data were included in the model, we set an additional constraint that spanned the sample age  $\pm 15$  Myr from 140–60 °C (e.g., Fraser et al. 2021). Constraint boxes were combined when multiple thermochronometers overlap in age. The final outputs from HeFTy are the good and acceptable fit *t-T* paths (Fig. S9) along with the weighted mean *t-T* path (Fig. 5).

To visualize the HeFTy results, we use nodal density plots that highlight regions in *t-T* space where thermal history paths overlap (Fig. S8). We overlay these density plots with the weighted mean path to highlight first-order cooling trends.

We describe the timing and rate of cooling through the temperature sensitivity windows that are directly constrained by the input data in our models. Sample Y11 is located less than 1 km from the Shannon fault, so we interpret young and dispersed single-grain dates in this sample to be caused by partial daughter loss during fault-related reheating (e.g., fluid flow). We therefore elected not to conduct thermal history modeling for this sample.

### 5.2. Modeling results

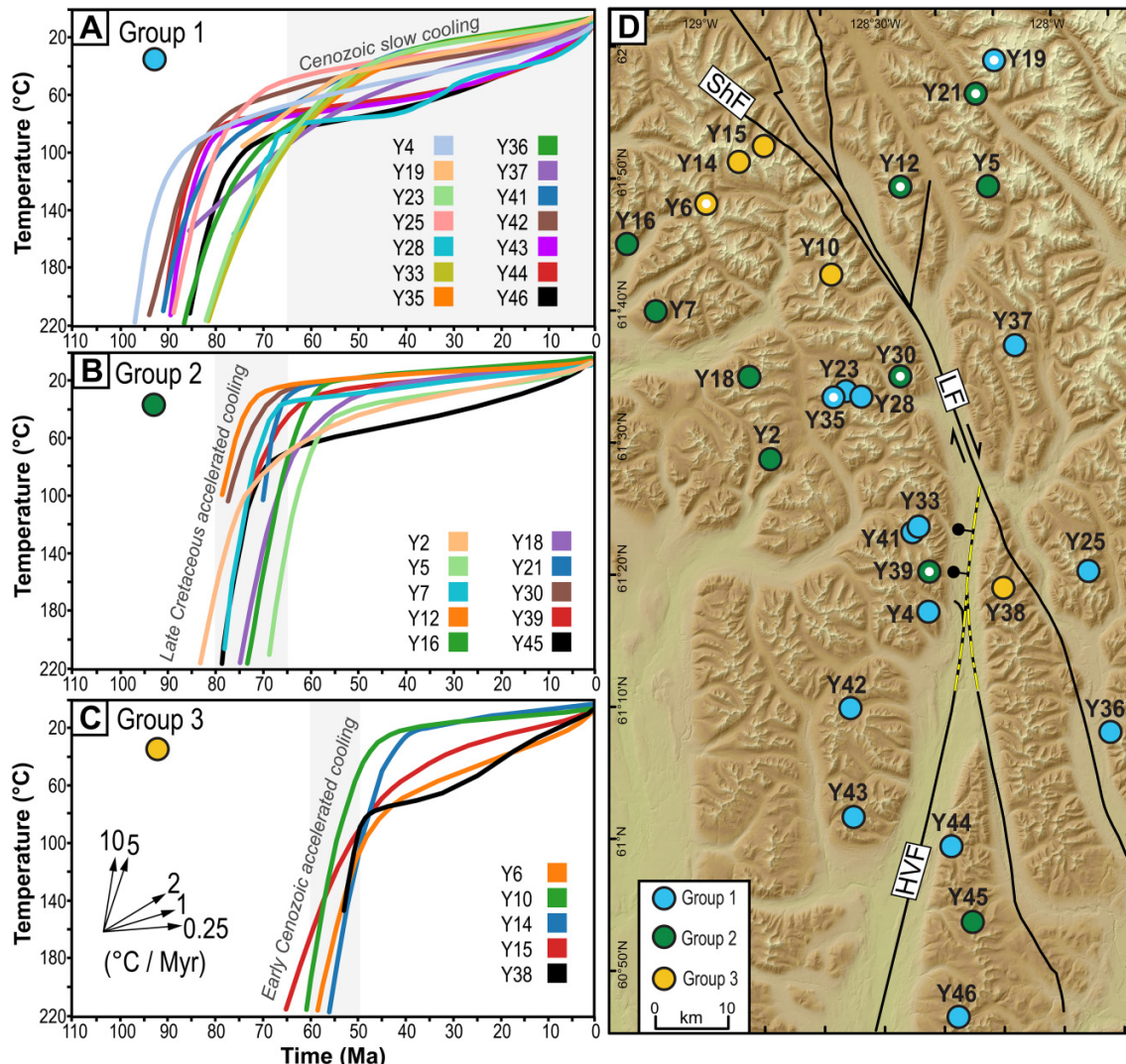
We use the weighted mean path as a representation of the thermal history revealed in each model herein (Fig. 5) and provide density plots (Fig. S8) and the HeFTy results (Fig. S9) for each individual sample model in the supplementary material. Examination of these plots revealed three distinct groups of thermal histories based on the timing and rate of cooling (Fig. 5A–5C). Group 1 thermal histories are characterized by slow cooling (<2 °C/Myr) from ~100 °C to surface temperatures since ca. 65 Ma (Fig. 5A). Group 2 thermal histories are characterized by accelerated cooling (>5 °C/Myr) between ca. 80 and 65 Ma (Fig. 5B). By ca. 55 Ma, all models in this group show slow cooling (<2 °C/Myr) from >80 °C to <40 °C. Group 3 thermal histories are characterized by accelerated cooling between ca. 60 and 50 Ma (Fig. 5C). Samples Y10, Y14, and Y38 all show rapid cooling (>10 °C/Myr) during this time. All samples in this group show a noticeable decrease in cooling rate to <2 °C/Myr by ca. 45 Ma.

## 6. Discussion

### 6.1. Spatial distribution of rock cooling

We show the spatial distribution of the three different thermal history groups by color coding the sample locations on the regional map (Fig. 5D). To further investigate the spatial pattern of rock cooling, we plot our thermochronometric data along swaths profiles that cross the faults in the Upper Hyland River Valley (Fig. 6) and a swath profile that parallels the faults to the west (Fig. 7). Thermal history group 1 comprises most samples in our study (Fig. 5D). Samples in this group are located throughout the entire study area but are most prevalent in the central and southern part and on both sides of the Logan and Hyland Valley faults (blue dots in Fig. 5D). For samples that have ZHe dates, many of these dates overlap, or slightly postdate, the intrusion ages of the Hyland, Tay River, and Tungsten plutonic suites (e.g., Y4, Y33, Y41, Y42, and Y43; Figs. 3, 5, and 6). This mid-Cretaceous cooling signal recorded in the ZHe data is gradually lost towards the north, where ZHe ages get progressively younger (Fig. 7). These data and thermal history models reflect emplacement and post-emplacement protracted cooling of plutons in the area. This is consistent with emplacement depths from plutons in the Upper Hyland River Valley of ~9–12 km as suggested by previous studies (e.g., Moynihan 2013). Due to the lack of ZHe data for some of our samples, the higher temperature cooling that results from shallow pluton emplacement has not been captured in all cases. However, AHe and AFT data from other samples (e.g., Y23, Y28, Y35, and Y37) constrain the low temperature portion of the cooling his-

**Fig. 5.** Summary of thermal history modeling results using the weighted mean  $t$ - $T$  path for each individual thermal history model. (A) Thermal history group 1 characterized by protracted Cenozoic cooling. (B) Thermal history group 2 characterized by a cooling phase ca. 80–65 Ma. (C) Thermal history group 3 characterized by a cooling phase ca. 60–50 Ma. (D) Map of samples color-coded by thermal history group and major faults. The location of the map area is shown in Fig. 2. Samples with a white dot have only one (U-Th)/He thermochronometer. The black and yellow dashed line shows the continuation of faults we infer based on our thermochronology data. The fault motion symbols show the kinematics of the faults we suggest were active ca. 60–50 Ma; see discussion in text. HVF—Hyland Valley fault, LF—Logan fault, and ShF—Shannon fault. The map projection in (D) is NAD 83 UTM Zone 9N.



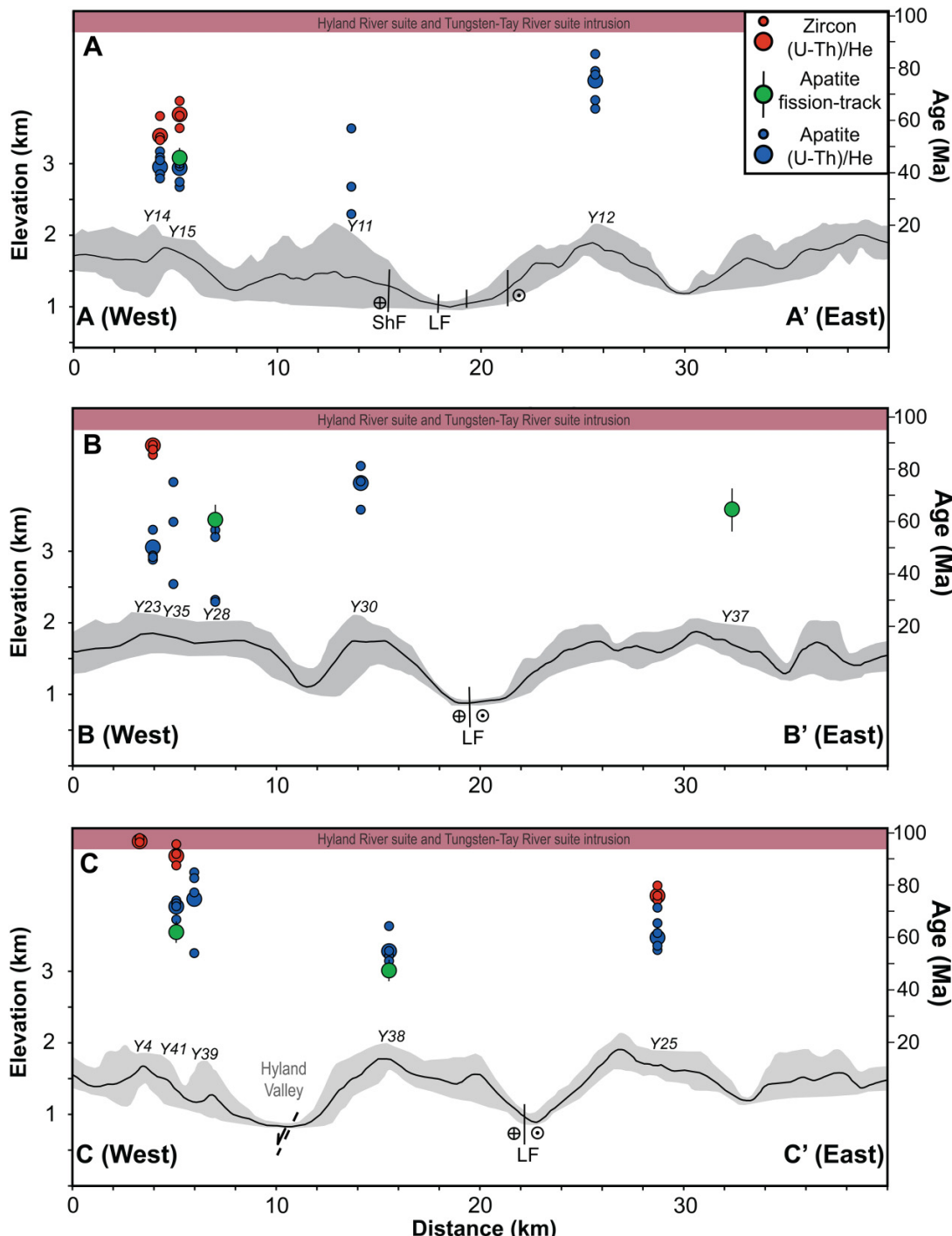
tory, characterized by protracted Cenozoic cooling (group 1; Fig. 5A).

Samples characterized by rapid cooling ca. 80–65 Ma (group 2; Fig. 5B) are primarily located in the north of the study area (green dots in Fig. 5D). Samples in this group are found on both sides of the Logan fault and at distances greater than 30 km west of the Shannon fault.

Samples characterized by rapid cooling ca. 60–50 Ma (group 3; Fig. 5C) are located within 20 km west of the Shannon and Hyland Valley faults (yellow dots in Fig. 5D). Samples near the Shannon fault (Y6, Y10, Y14, Y15) have relatively young (latest Paleocene–Eocene) cooling ages, and AHe ages noticeably increase (Late Cretaceous–early Paleocene) east of the fault

(Figs. 5B and 6A). The AHe age from sample Y12 (75.6 Ma) is older than AHe, AFT, and ZHe ages from samples Y14 and Y15 located ~5 km west of the Shannon fault (Fig. 6A). In the southern part of the study area, an additional sample (Y38) belongs to thermal history group 3 and is located ~4 km west of the Logan fault (Fig. 5D). The swath profile (Fig. 6C) shows that from west to east, AHe ages decrease across a suspected fault located in the Hyland Valley and then increase slightly across the Logan fault. The west–east decreasing ages across the Hyland Valley is also seen in our AFT ages (Fig. 6C). This observed age trend supports the existence of a fault located between the northern end of the Hyland Valley fault and the Logan fault (Fig. 5D).

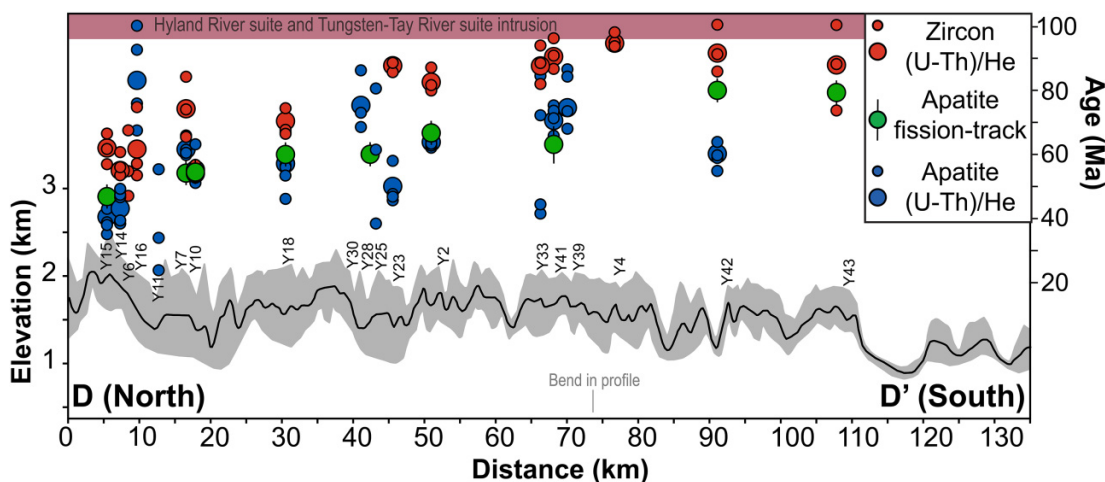
**Fig. 6.** Swath profiles across the (A) northern, (B) central, and (C) southern Upper Hyland Valley. Swaths are 5 km wide and include samples located proximal to the main structures in the Upper Hyland River Valley. The location of each profile is shown in Fig. 3A. Large circles are sample ages (when calculated) and small circle are single-grain dates. The red shaded bar highlights the time of pluton emplacement in the Upper Hyland River Valley. LF—Logan fault and ShF—Shannon fault.



The juxtaposition between samples from different cooling history groups and faults in our study area suggests fault-controlled rock exhumation. The northern part of the Hyland Valley fault juxtaposes samples from groups 1 (Y4, Y33, and Y41) and 2 (Y39) to the west with group 3 (Y38) to the east and contrasts Cretaceous–early Paleocene cooling ages to the west with latest Paleocene–Eocene ages to the east (Figs. 3B,

5D, and 6C). Across the Hyland Valley fault, samples Y42, Y43, Y44, Y45, and Y46 all exhibit cooling rates  $<2\text{ }^{\circ}\text{C}/\text{Myr}$  since ca. 70 Ma (group 1) and all but Y45 show accelerated cooling prior to 90 Ma (Fig. 5). This indicates that dip-slip motion on the Hyland Valley fault in the southern part of the study area has not occurred since  $\sim 110$  Ma. We suggest that normal displacement occurred along an inferred fault east of the Hyland

**Fig. 7.** Swath profile along the western side of the Logan fault. Swath is 5 km wide. Large circles are sample ages (when calculated) and small circle are single-grain dates. The location of the profile is shown in Fig. 3A. The red shaded bar indicates the time of pluton emplacement in the Upper Hyland River Valley.



Valley fault that likely connects with the Logan fault further north (yellow dashed line in Figs. 3 and 5D, block model in Fig. 8C). More samples from the inferred footwall of this fault (east side) are needed to further resolve the southern extent of normal displacement.

Across the Shannon and Logan faults in the northern part of the study, cooling ages increase from west to east (Fig. 6A) and these faults separate samples in group 1 from samples in the other two groups (Fig. 5D). In contrast, we do not observe evidence of differential cooling across the Logan fault. Samples Y28 and Y37 have AFT ages that overlap within uncertainty (Figs. 3 and 6B) and both belong to group 1 (Fig. 5). This suggests that differential cooling has not occurred across the Logan fault. We therefore suggest that the Shannon fault, not the Logan fault, controls the differential cooling we document in the northern part of our study area during the early Cenozoic (Figs. 5 and 8C).

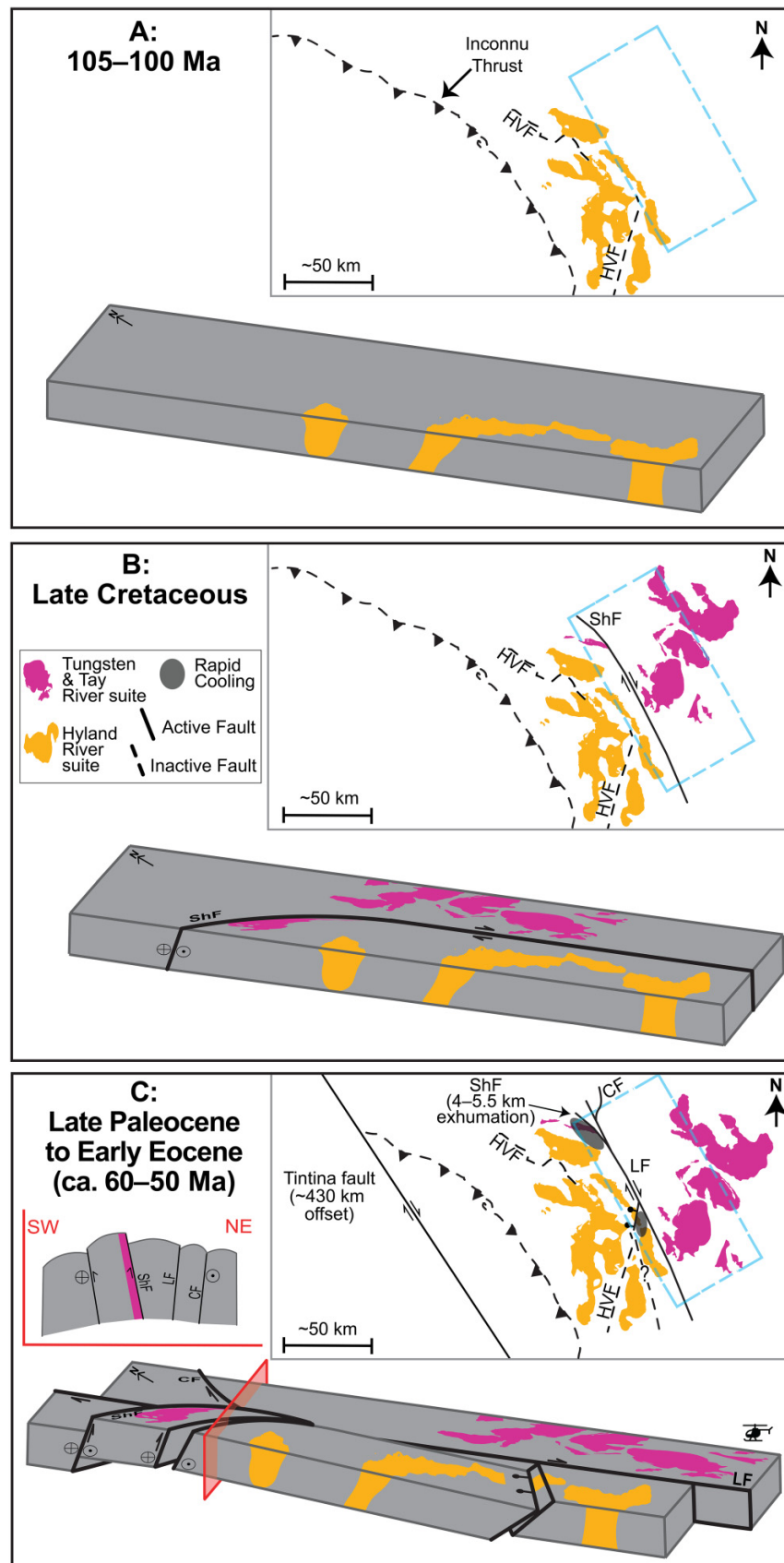
## 6.2. Early Cenozoic faulting in the Upper Hyland River Valley

The spatial pattern suggests that cooling is the result of dip-slip faulting along the Shannon fault and along the speculated fault east of the Hyland Valley fault that occurred ca. 60–50 Ma (Fig. 5D). We suggest that rock cooling in sample Y38 is caused by tectonic exhumation of the footwall of this unnamed fault, which we interpret as a normal fault. Based on our new data and thermal history modeling, we suggest that this fault continues north where it likely connects with the Logan fault (Fig. 5D). Rock cooling in samples Y6, Y10, Y14, and Y15 is caused by rock uplift and erosional exhumation adjacent to the Shannon fault. In our model, the Shannon fault is part of a restraining bend, driving localized uplift and subsequent exhumation ca. 60–50 Ma. Assuming geothermal gradients between 25 and 35 °C/km (e.g., O’Sullivan and Lane 1997; McKay et al. 2021), this equates to ~4–5.5 km of exhumation (Table S7).

We suggest that the two faults, connected by the dextral strike-slip along the Logan fault, resulted in northwest-directed translation of the western block (Fig. 8). This is supported by the south to north decrease in cooling age and increase in topography observed in the swath profile of this western block (Fig. 7). The similar ages across the central portion of the Logan fault suggest that displacement is mostly strike-slip (Fig. 6). Faults oblique to the strike of the Logan fault were active as dip-slip faults, resulting in contrasting thermal histories across these structures.

We propose the following tectonic model for the mid-Cretaceous–Eocene tectonic evolution of the Upper Hyland River Valley (Fig. 8). In the Early Cretaceous, Hyland suite plutons were emplaced east of the present-day trace of the Logan fault (Fig. 8A). In the Late Cretaceous, Tungsten suite and Tay River suite plutons were emplaced. This included the ca. 100–98 Ma Shannon pluton and coeval ductile shearing along the Shannon fault (Tollefson et al. 2023). In our model, the Shannon fault extended southeast along the present-day trace of the Logan fault (Fig. 8B). Initial dextral strike-slip faulting took place ca. 98.5 Ma, during the emplacement of the eastern part of the Shannon pluton. The magnitude of displacement during this phase of activity is unknown. In the late Paleocene–early Eocene, the fault system was active and propagated to the north during further dextral strike-slip displacement (Figs. 3 and 8C). The Shannon fault acted as a fault stepover or a restraining bend that caused localized exhumation (Fig. 8C). Close to the surface, restraining bends tend to widen into a network of multiple smaller structures (e.g., Cunningham and Mann 2007; Woodcock and Fischer 1986). Other smaller faults have been mapped south of the Shannon pluton (Fig. 3A). Thus, the resulting contractional strike-slip duplex or positive flower structure may have caused localized exhumation accommodated by the present-day Shannon fault (Figs. 3A). We therefore suggest a flower structure as a possible model to explain the pattern of cooling we observe in our thermochronology data based on the locations

**Fig. 8.** Schematic maps and block diagrams showing the mid-Cretaceous to Eocene tectonic evolution of the Upper Hyland River Valley area in the Logan Mountains. The view for the block diagrams is to the northeast. The blue dashed box in each map shows the areal extent shown in the corresponding block diagram. The red plane in the block diagram in panel (C) shows the location of the schematic cross-section above the block diagram. Note: block diagrams are not to scale. CF—Connector fault, HVF—Hyland Valley fault, LF—Logan fault, and ShF—Shannon fault.



and orientations of faults in the area (Fig. 8C). However, a high-density sampling approach across other faults north and south of the Shannon pluton would be needed to confirm this interpretation and map out the spatial extend of such a contractional structure (Fig. 3A). In our model, the suggested fault east of the Hyland Valley fault was active as a normal fault during the late Paleocene–early Eocene and likely accommodated <2 km of exhumation (Fig. 8C).

### 6.3. Tectonic implications

Our results build on previous studies documenting the role of fault stepovers and restraining bends in driving localized exhumation along strike-slip faults in the North American Cordillera. For example, the San Bernardino Mountains in southern California have been uplifted and exhumed as restraining bends along the San Andreas fault (Spotila et al. 1998, 2001, 2020; Niemi et al. 2013). Miocene–recent exhumation rates derived from thermochronology data range from ~0.05 mm/year to as high as 7 mm/year (Blythe et al. 2000; Spotila et al. 2001, 2007). These exhumation rates are in good agreement with our calculated rates for rocks from the Shannon pluton, which range ~0.4–0.5 mm/year (Table S7). Mount Denali in central Alaska is another well-documented example of building high topography and rapid rock exhumation in a restraining bend (e.g., Benowitz et al. 2021). Located in a restraining bend along the Denali fault, Miocene-to-recent uplift rates at Mount Denali are suggested to be ~1.5 mm/year (Fitzgerald et al. 1995; Lease et al. 2016). These studies demonstrate the role of localized transpression along continental-scale strike-slip faults with >100 km of displacement in driving localized late Cenozoic exhumation in the North American Cordillera. Our results show similar processes occur on the scale of regional faults (<100 km of displacement) and that these faults should be investigated as kinematic drivers for spatial variations in rock exhumation and landscape evolution in the Northern Canadian Cordillera.

Fault-controlled exhumation in the Logan Mountains occurred at the same time as the Tintina fault is suggested to have been active (Fig. 8C; e.g., Gabrielse et al. 2006; Monger and Gibson 2019). The Logan fault strikes roughly parallel to the Tintina fault and would therefore be favorably oriented to be activated under the same stress field. Our data suggest that faulting in the Upper Hyland River Valley likely ceased in the early Eocene, possibly due to strain localization along the Tintina fault that accommodated ~430 km of dextral slip (Murphy et al. 1995; Murphy and Mortensen 2003; Gabrielse et al. 2006; Busby et al. 2023).

While we cannot directly constrain the timing and magnitude of strike-slip displacement on the Logan fault, our proposed kinematic model requires a phase of late-Paleocene–early Eocene strike-slip to explain the observed localized cooling pattern (Fig. 8C). Our data support Cenozoic reactivation of the Shannon fault. Shear band fabrics (Figs. 4C and 4D) and fractured mylonite (Fig. 4B) adjacent to the Shannon fault indicate ductile and brittle phases of deformation; the ductile phase accommodated dextral translation while the kinematic significance of the brittle deformation is not constrained by field observations. The evidence provided here

for reactivation of the Shannon fault suggests that this brittle deformation took place during the late Paleocene–early Eocene and is consistent with previous studies that have documented Cenozoic reactivation of Cretaceous faults in the Northern Canadian Cordillera. For example, three distinct phases of slip have been documented on the Big Creek fault using carbonate U-Pb and illite K-Ar dating of fault-generated materials. The earliest slip (ca. 112–105 Ma) was coeval with the emplacement of the Whitehorse plutonic suite (Fig. 1), and later reactivation occurred at 79–72 and 50–45 Ma (Allan et al. 2013; Friend et al. 2017; Mottram et al. 2020, 2024). The Teslin fault is documented as a Cretaceous dextral fault (Gabrielse 1985; Gabrielse et al. 2006) that was active again in the Cenozoic. Paleogene AHe and AFT ages from the Whitehorse Trough, which is bounded to the east by the Teslin fault, have been interpreted to reflect fault-controlled block uplift and rapid exhumation (Kellett et al. 2023). Paleogene displacement on the Teslin fault has also been suggested due to the presence of ductile fabrics in a ca. 57 Ma pluton near the trace of the Teslin fault (Mihalynuk et al. 2006). White et al. (2012) suggested the possibility of Jurassic movement on this structure. The Llewellyn fault, part of the Llewellyn fault-Tally Ho shear zone in northern British Columbia and southern Yukon, is suggested to have been periodically active since the late Triassic (Mihalynuk et al. 1999). Illite  $^{40}\text{Ar}$ - $^{39}\text{Ar}$  dating from epithermal veins near this fault zone are interpreted to reflect dextral reactivation of the Llewellyn fault ca. 50 Ma (Millonig et al. 2017).

## 7. Conclusions

We present new low-temperature thermochronology data from the Logan Mountains, southeastern Yukon, Canada. Cooling ages and thermal history modeling suggest that the most recent phase of cooling in the area occurred ca. 60–50 Ma. This cooling phase is documented to the west of the Shannon fault and in the footwall of an inferred fault in the Hyland River valley. Based on this spatial pattern, we propose a kinematic model where dextral activation of the Logan fault resulted in localized transpression along the obliquely striking Shannon fault (Fig. 8). We show ~4–5.5 km of localized exhumation adjacent to the Shannon fault that is likely part of a contractional flower structure. Cenozoic displacement on the Logan fault was coeval with dextral motion along the Tintina fault ca. 60 Ma, and faulting in the Upper Hyland River Valley likely ceased in the early Eocene due to strain localization on the Tintina fault.

## Acknowledgements

The authors wish to acknowledge the peoples of the Kaska First Nations, on whose traditional territories the study area is located. Samples for this study were collected by DPM, Rosie Cobbett, and Kirsten Rasmussen, and were provided by the Yukon Geological Survey. We thank Jeremy Powell, Dave Schneider, and one anonymous reviewer for their constructive feedback on the manuscript. JP wishes to thank Birk Härtel, Dave Whipp, Uwe Kröner, Kyle Tollefson, and Paul O’Sullivan for their insightful comments that greatly shaped

the direction of this research. This research was supported by Natural Resource Canada (NRCan)'s GeoMapping for Energy and Minerals-GeoNorth program, as well as an NRCan Research Affiliate Bursary to Padgett. This is Yukon Geological Survey Contribution #071.

## Article information

### History dates

Received: 9 October 2024

Accepted: 17 December 2024

Accepted manuscript online: 21 January 2025

Version of record online: 31 March 2025

### Copyright

© 2025 Authors Padgett, Enkelmann, Stephan; Yukon Geological Survey; and His Majesty the King in Right of Canada, as represented by the Minister of Natural Resources. This work is licensed under a [Creative Commons Attribution 4.0 International License](#) (CC BY 4.0), which permits unrestricted use, distribution, and reproduction in any medium, provided the original author(s) and source are credited.

### Data availability

All data presented in this study are available in the supplementary files.

## Author information

### Author ORCIDs

Joel Padgett <https://orcid.org/0009-0009-2074-1918>

Eva Enkelmann <https://orcid.org/0000-0002-1988-0760>

Dawn A. Kellett <https://orcid.org/0000-0002-4558-4703>

David P. Moynihan <https://orcid.org/0000-0003-0156-4775>

Tobias Stephan <https://orcid.org/0000-0002-9290-014X>

### Author notes

Eva Enkelmann and Dawn A. Kellett served as Associate Editors at the time of manuscript review and acceptance; peer review and editorial decisions regarding this manuscript were handled by another editorial board member.

### Author contributions

Conceptualization: EE, DPM

Data curation: JP, EE

Formal analysis: JP, EE, DAK, DPM, TS

Funding acquisition: JP, EE, DAK, DPM

Investigation: JP, EE

Methodology: EE

Project administration: EE, DAK

Resources: DPM

Software: TS

Visualization: JP, TS

Writing – original draft: JP

Writing – review & editing: JP, EE, DAK, DPM, TS

### Competing interests

The authors declare there are no competing interests.

### Funding information

This research was funded by Canada's GEM-GeoNorth Initiative and Natural Sciences and Engineering Research Council of Canada (NSERC) RGPIN-2018-03932 (EE) and NRS-2018-517959 (EE). JP is grateful for financial support from NRCan's Geological Survey of Canada through the Research Affiliate Program, the Yukon Foundation, the University of Calgary, and the Government of Alberta through the Alberta Graduate Excellence Scholarship program.

### Supplementary material

Supplementary data are available with the article at <https://doi.org/10.1139/cjes-2024-0147>.

### References

- Abbott, J.G., Gordey, S.P., and Tempelman-Kluit, D.J. 1986. Setting of Stratiform, Sediment Hosted Lead-Zinc Deposits in Yukon and Northeastern British Columbia. In *Mineral deposits of Northern Cordillera, Special Volume 37*. Edited by J.A. Morin. Canadian Institute of Mining and Metallurgy. pp. 1–18.
- Allan, M.M., Mortensen, J.K., Hart, C.J.R., Bailey, L.A., Sánchez, M.G., Ciolkiewicz, W., et al. 2013. Magmatic and metallogenic framework of West-Central Yukon and Eastern Alaska. In *Tectonics, Metallogeny, and Discovery: The North American Cordillera and Similar Accretionary Settings*: SEG, Special Publication, Vol. 17. Edited by M. Colpron, T. Bissig, B. Rusk and J. Thompson. pp. 111–168.
- Benowitz, J.A., Cooke, M.L., Terhune, P.J., Herreid, S., Bemis, S.P., Toeneboehn, K., et al. 2021. Why is Denali (6,194 m) so big? Caught inside the tectonic wake of a migrating restraining bend. *Terra Nova*, **34**(2): 123–136. doi:[10.1111/ter.12571](https://doi.org/10.1111/ter.12571).
- Beranek, L.P., and Mortensen, J.K. 2011. The timing and provenance record of the Late Permian Klondike orogeny in northwestern Canada and arc-continent collision along western North America. *Tectonics*, **30**. doi:[10.1029/2010TC002849](https://doi.org/10.1029/2010TC002849).
- Blythe, B., Farley, & Fielding. 2000. Structural and topographic evolution of the Central Transverse Ranges, California, from apatite fission-track, (U-Th)/He and Digital Elevation Model analyses. *Basin Research*, **12**(2): 97–114. doi:[10.1046/j.1365-2117.2000.00116.x](https://doi.org/10.1046/j.1365-2117.2000.00116.x).
- Busby, C.J., Pavlis, T.L., Roeske, S.M., and Tikoff, B. 2023. The North American Cordillera during the mesozoic to Paleogene: Selected questions and controversies. In *Laurentia: turning points in the evolution of a continent*: Geological Society of America Memoir 220. Edited by S.J. Whitmeyer, M.L. Williams, D.A. Kellett and B. Tikoff. pp. 635–658. doi:[10.1130/2022.21220\(31\)](https://doi.org/10.1130/2022.21220(31)).
- Clark, A.D. 2017. Tectonometamorphic history of mid-crustal rocks at Aishihik Lake, southwest Yukon. Master's thesis, Simon Fraser University.
- Colpron, M., Crowley, J.L., Gehrels, G., Long, D.G., Murphy, D.C., Beranek, L., and Bickerton, L. 2015. Birth of the northern Cordilleran orogen, as recorded by detrital zircons in Jurassic synorogenic strata and regional exhumation in Yukon. *Lithosphere* **7**: 541–562. doi:[10.1130/L451.1](https://doi.org/10.1130/L451.1).
- Colpron, M., Sack, P.J., Crowley, J.L., Beranek, L.P., and Allan, M.M. 2022. Late Triassic to Jurassic magmatic and tectonic evolution of the intermontane terranes in Yukon, northern Canadian Cordillera: Transition from arc to syn-collisional magmatism and post-collisional lithospheric delamination. *Tectonics*, **41**(2): 1–32. doi:[10.1029/2021tc007060](https://doi.org/10.1029/2021tc007060).
- Cunningham, W.D., and Mann, P. 2007. Tectonics of strike-slip restraining and releasing bends. *Geological Society, London, Special Publications*, **290**: 1–12. doi:[10.1144/sp290.1](https://doi.org/10.1144/sp290.1).
- Damant, K.A., Enkelmann, E., and Jess, S. 2023. Prolonged post-orogenic extension in the southeastern Canadian cordillera: Miocene reactivation of the Columbia River Fault. *Tectonophysics*, **850**: 229763. doi:[10.1016/j.tecto.2023.229763](https://doi.org/10.1016/j.tecto.2023.229763).
- Donelick, R.A., Ketcham, R.A., and Carlson, W.D. 1999. Variability of apatite fission-track annealing kinetics; II, crystallographic orienta-

- tion effects. *American Mineralogist*, **84**(9): 1224–1234. doi:[10.2138/am-1999-0902](#).
- Driver, L.A., Creaser, R.A., Chacko, T., and Erdmer, P. 2000. Petrogenesis of the Cretaceous Cassiar Batholith, Yukon–British Columbia, Canada: Implications for magmatism in the North American Cordilleran Interior. *Geological Society of America Bulletin*, **112**(7): 1119–1133. doi:[10.1130/0016-7606\(2000\)112](#).
- Estève, C., Audet, P., Schaeffer, A.J., Schutt, D.L., Aster, R.C., and Cubley, J.F. 2020. Seismic evidence for craton chiseling and displacement of lithospheric mantle by the Tintina Fault in the northern Canadian Cordillera. *Geology*, **48**: 1120–1125. doi:[10.1130/g47688.1](#).
- Evenchick, C.A., McMechan, M.E., McNicoll, V.J., and Carr, S.D. 2007. A synthesis of the Jurassic–Cretaceous tectonic evolution of the Central and southeastern Canadian Cordillera: Exploring links across the orogen. In *Special Paper 433: Whence the mountains? Inquiries into the Evolution of Orogenic Systems: A Volume in Honor of Raymond A. Price*. pp. 117–145. doi:[10.1130/2007.2433\(06\)](#).
- Farley, K.A. 2002. (U-Th)/He dating: Techniques, calibrations, and applications. *Reviews in Mineralogy and Geochemistry*, **47**: 819–844. doi:[10.2138/rmg.2002.47.18](#).
- Finzel, E.S., Trop, J.M., Ridgway, K.D., and Enkelmann, E. 2011. Upper plate proxies for flat-slab subduction processes in southern Alaska. *Earth and Planetary Science Letters*, **303**: 348–360. doi:[10.1016/j.epsl.2011.01.014](#).
- Fitzgerald, P.G., Sorkhabi, R.B., Redfield, T.F., and Stump, E. 1995. Uplift and denudation of the central Alaska Range: A case study in the use of apatite fission track thermochronology to determine absolute uplift parameters. *Journal of Geophysical Research: Solid Earth*, **100**: 20175–20191. doi:[10.1029/95JB02150](#).
- Flowers, R.M., Ketcham, R.A., Enkelmann, E., Gautheron, C., Reiners, P.W., Metcalf, J.R., et al. 2022b. (U-Th)/He chronology: Part 2. Considerations for evaluating, integrating, and interpreting conventional individual aliquot data. *GSA Bulletin*, **135**: 137–161. doi:[10.1130/b36268.1](#).
- Flowers, R.M., Ketcham, R.A., Shuster, D.L., and Farley, K.A. 2009. Apatite (U-Th)/He thermochronometry using a radiation damage accumulation and annealing model. *Geochimica et Cosmochimica acta*, **73**: 2347–2365. doi:[10.1016/j.gca.2009.01.015](#).
- Flowers, R.M., Zeitler, P.K., Danišík, M., Reiners, P.W., Gautheron, C., Ketcham, R.A., et al. 2022a. (U-Th)/He chronology: Part 1. Data, uncertainty, and reporting. *GSA Bulletin*, **135**: 104–136. doi:[10.1130/b36266.1](#).
- Fraser, K.I., Enkelmann, E., Jess, S., Gilbert, H., and Grieco, R. 2021. Resolving the Cenozoic History of Rock Exhumation along the Central Rocky Mountain Trench using Apatite Low-Temperature Thermochronology. *Tectonics*, **40**(10). doi:[10.1029/2021tc006847](#).
- Friend, M.A., Allan, M.M., and Hart, C.J.R. 2017. New contributions to the bedrock geology of the Mount Freeland district, Dawson Range, Yukon (NTS 115I/2, 6 and 7). Edited by K.E. MacFarlane. Yukon Exploration and Geology 2017: Whitehorse, Yukon Geological Survey. pp. 47–68.
- Gabrielse, H. 1985. Major dextral transcurrent displacements along the northern Rocky Mountain Trench and related lineaments in north-central British Columbia. *Geological Society of America Bulletin*, **96**: 1–14. doi:[10.1130/0016-7606\(1985\)96%3c1:MDTDAT%3e2.0.CO;2](#).
- Gabrielse, H. 1991. Structural styles, In *Geology of the Cordilleran Orogen in Canada*. Edited by H. Gabrielse and C.J. Yorath. Geological Survey of Canada Geology of Canada 4. pp. 571–675.
- Gabrielse, H., Murphy, D.C., and Mortensen, J.K. 2006. Cretaceous and Cenozoic dextral orogen-parallel displacements, magmatism, and paleogeography, north-central Canadian Cordillera. In *Paleogeography of the North American Cordillera: Evidence For and Against Large-Scale Displacements*, Geological Survey of Canada Special Paper 46. pp. 255–276.
- Gaidies, F., Morneau, Y.E., Petts, D.C., Jackson, S.E., Zagorevski, A., and Ryan, J.R. 2020. Major and trace element mapping of garnet: unravelling the conditions, timing and rates of metamorphism of the Snowcap assemblage, west-central Yukon. *Journal of Metamorphic Geology*, **00**: 1–32. doi:[10.1111/jmg.12562](#).
- Gordy, S.P., and Anderson, R.G. 1993. Evolution of the northern Cordilleran miogeocline, Nahanni map area (105), Yukon and Northwest Territories. In *Geological Survey of Canada Memoir 428*. p. 214.
- Guenther, W.R. 2021. Implementation of an Alpha Damage Annealing Model for Zircon (U-Th)/He thermochronology with comparison to a zircon fission track annealing model. *Geochemistry, Geophysics, Geosystems*, **22**(2): 1–16. doi:[10.1029/2019gc008757](#).
- Guenther, W.R., Reiners, P.W., Ketcham, R.A., Nasdala, L., and Gester, G. 2013. Helium diffusion in natural zircon: radiation damage, anisotropy, and the interpretation of zircon (U-Th)/He thermochronology. *American Journal of Science*, **313**(3): 145–198. doi:[10.2475/03.2013.01](#).
- Harrison, T.M., and Zeitler, P.K. 2005. Fundamentals of noble gas thermochronometry. *Reviews in Mineralogy and Geochemistry*, **58**: 123–149. doi:[10.2138/rmg.2005.58.5](#).
- Hart, C.J., Goldfarb, R.J., Lewis, L.L., and Mair, J.L. 2004. The northern cordilleran Mid-Cretaceous plutonic province: Ilmenite/magnetite-series granitoids and intrusion-related mineralisation. *Resource Geology*, **54**(3): 253–280. doi:[10.1111/j.1751-3928.2004.tb00206.x](#).
- Härtel, B., and Enkelmann, E. 2024. The daughter-parent plot: a tool for analyzing thermochronological data. *Geochronology*, **6**(3): 429–448. doi:[10.5194/gchron-6-429-2024](#).
- Härtel, B., Jonckheere, R., Krause, J., and Ratschbacher, L. 2022. Spurious age-eU associations in thermochronological data. *Earth and Planetary Science Letters*, **599**: 117870. doi:[10.1016/j.epsl.2022.117870](#).
- Heffernan, R.S. 2004. Temporal, geochemical, isotopic, and metallogenetic studies of mid-Cretaceous magmatism in the Tintina Gold Province, southeastern Yukon and southwestern Northwest Territories, Canada. Unpublished M.Sc. thesis, University of British Columbia, Vancouver, BC. 83p.
- Hurford, A.J., and Green, P.F. 1983. The zeta age calibration of fission-track dating. *Chemical Geology*, **41**: 285–317. doi:[10.1016/s0009-2541\(83\)80026-6](#).
- Hyndman, R.D., Flück, P., Mazzotti, S., Lewis, T.J., Ristau, J., and Leonard, L. 2005. Current tectonics of the northern Canadian Cordillera. *Canadian Journal of Earth Sciences*, **42**(6): 1117–1136. doi:[10.1139/e05-023](#).
- Kellett, D.A., Coutand, I., Zagorevski, A., Grujic, D., Dewing, K., and Beranek, L. 2023. Whitehorse Trough records late Triassic–Cretaceous accretionary orogenesis in the northern Canadian Cordillera via detrital mineral thermochronometry. *Canadian Journal of Earth Sciences*, **61**(2): 223–247. doi:[10.1139/cjes-2023-0082](#).
- Ketcham, R.A. 2005. Forward and inverse modeling of low-temperature thermochronometry data. *Reviews in Mineralogy and Geochemistry*, **58**(1): 275–314. doi:[10.2138/rmg.2005.58.11](#).
- Ketcham, R.A. 2024. Thermal history inversion from thermochronometric data and complementary information: new methods and recommended practices. *Chemical Geology*, **653**: 122042. doi:[10.1016/j.chemgeo.2024.122042](#).
- Ketcham, R.A., Carter, A., Donelick, R.A., Barbarand, J., and Hurford, A.J. 2007. Improved modeling of fission-track annealing in apatite. *American Mineralogist*, **92**(5–6): 799–810. doi:[10.2138/am.2007.2281](#).
- Laslett, G.M., Green, P.F., Duddy, I.R., and Gleadow, A.J.W. 1987. Thermal annealing of fission tracks in apatite 2. A quantitative analysis. *Chemical Geology*, **65**: 1–13. doi:[10.1016/0168-9622\(87\)90057-1](#).
- Lease, R.O., Haeussler, P.J., and O’Sullivan, P. 2016. Changing exhumation patterns during Cenozoic growth and glaciation of the Alaska Range: Insights from detrital thermochronology and geochronology. *Tectonics*, **35**: 934–955. doi:[10.1002/2015TC004067](#).
- Mair, J.L., Hart, C.J.R., and Stephens, J.R. 2006. Deformation history of the northwestern Selwyn Basin, Yukon, Canada: implications for orogen evolution and mid-Cretaceous magmatism. *Geological Society of America Bulletin*, **118**: 304–323. doi:[10.1130/b25763.1](#).
- McKay, R., Enkelmann, E., Hadlari, T., Matthews, W., and Mouthereau, F. 2021. Cenozoic exhumation history of the eastern margin of the northern Canadian Cordillera. *Tectonics*, **40**. doi:[10.1029/2020tc006582](#).
- Mihalynuk, M.G., Friedman, R.M., and Devine F Heaman, L.M. 2006. Protolith age and deformation history of the Big Salmon complex, relicts of a Paleozoic continental arc in northern British Columbia. In *Paleozoic Evolution and Metallogeny of Pericratonic Terranes at the Ancient Pacific Margin of North America, Canadian and Alaskan Cordillera*. Edited by M. Colpron and J.L. Nelson. Geological Association of Canada, Special Paper 45. pp. 179–200.
- Mihalynuk, M.G., Mountjoy, K.J., Smith, M.T., Currie, L.D., Gabites, J.E., Tipper, H.W., et al. 1999. Geology and mineral resources of the Tagish Lake area (NTS 104 M/8, 9, 10E, 15 and 104 N/12 W), northwestern British Columbia. British Columbia Ministry of Energy and Mines, Energy and Minerals Division, Geological Survey Branch, Bulletin 105. p. 217.

- Millonig, L.J., Beinlich, A., Raudsepp, M., Devine, F., Archibald, D.A., Linnen, R.L., and Groat, L.A. 2017. The Engineer Mine, British Columbia: An example of epithermal Au-Ag mineralization with mixed alkaline and subalkaline characteristics. *Ore Geology Reviews*, **83**: 235–257. doi:[10.1016/j.oregeorev.2016.12.023](https://doi.org/10.1016/j.oregeorev.2016.12.023).
- Monger, J.W.H., and Gibson, H.D. 2019. Mesozoic-Cenozoic deformation in the Canadian Cordillera: The record of a “Continental bulldozer”? *Tectonophysics*, **757**: 153–169. doi:[10.1016/j.tecto.2018.12.023](https://doi.org/10.1016/j.tecto.2018.12.023).
- Mortensen, J.K., Hart, C.J.R., Murphy, D.C., and Heffernan, S. 2000. Temporal evolution of Early and mid-Cretaceous magmatism in the Tintina Gold Belt, in: Edited by T. Tucker, and M.J. Smith . The Tintina Gold Belt: Concepts, Exploration and Discoveries. British Columbia and Yukon Chamber of Mines Special, Volume 2, pp. 49–57.
- Mottram, C.M., Kellett, D.A., Barresi, T., Zwingmann, H., Friend, M., Todd, A., and Percival, J.B. 2020. Syncing fault rock clocks: Direct comparison of U-Pb carbonate and K-Ar illite fault dating methods. *Geology*, **48**(12): 1179–1183. doi:[10.1130/g47778.1](https://doi.org/10.1130/g47778.1).
- Mottram, C.M., Kellett, D.A., Barresi, T., Chapman, G.G., and Halle, J. 2024. Tracking the porphyry-epithermal mineralization transition using U-Pb carbonate dating. *Geology*. doi:[10.1130/g52211.1](https://doi.org/10.1130/g52211.1).
- Moynihan, D. 2016. Stratigraphy and structural geology of the upper Hyland River area (parts of 105H/8, 105H/9), southeast Yukon. Yukon Exploration and Geology 2015. pp. 187–206.
- Moynihan, D. 2017. Progress report on geological mapping in the upper Hyland River region of southeastern Yukon (parts of NTS 105H/08, 09, 10, 15, 16 and 105I/02). Edited by K.E. MacFarlane and L.H. Weston. Yukon Exploration and Geology. pp. 163–180.
- Moynihan, D.P. 2013. A preliminary assessment of low pressure, amphibolite-facies metamorphism in the upper Hyland River area (NTS 105H), southeast Yukon. In Yukon Exploration and Geology 2012. Edited by K.E. MacFarlane, M.G. Nordling and P.J. Sack. Yukon Geological Survey. pp. 99–114.
- Murphy, D.C. 1997. Geology of the McQuesten River Region, Northern McQuesten and Mayo Map Areas, Yukon Territory (115P/14,15,16; 105 M/13, 14). Exploration and Geological Services Division, Yukon, Indian and Northern Affairs Canada Bulletin, 6, 122.
- Murphy, D.C., and Mortensen, J.K. 2003. Late Paleozoic and Mesozoic features constrain displacement on Tintina fault and limit large-scale orogen-parallel displacement in the northern Cordillera. Geological Association of Canada, Mineral Association of Canada and Society of Economic Geologists, Program with Abstracts, 28. p. 151.
- Murphy, D.C., Mortensen, J.K., and Bevier, M.L. 1995. U-Pb and K-Ar geochronology of Cretaceous and Tertiary intrusions, western Selwyn basin, and implications for the structural and metallogenic evolution of central Yukon, in: Program with Abstracts. Presented at the Geological Association of Canada Mineralogical Association of Canada Annual Meeting, 74.
- Murphy, D.C., Mortensen, J.K., Piercey, S.J., Orchard, M.J., and Gehrels, G.E. 2006. Mid-Paleozoic to Early Mesozoic tectono-stratigraphic evolution of the Yukon-Tanana and Slide Mountain terranes and affiliated overlap assemblages, Finlayson Lake massive sulphide district, southeastern Yukon. In Paleozoic Evolution and Metallogeny of Pericratonic Terranes at the Ancient Pacific margin of North America, Canadian and Alaskan Cordillera. Edited by M. Colpron and J.L. Nelson. Geological Association of Canada, Special Paper 45. pp. 75–105.
- Nelson, J., and Colpron, M. 2007. Tectonics and Metallogeny of the British Columbia, Yukon, and Alaskan Cordillera, 1.8 Ga to the present. In Mineral Deposits of Canada: A Synthesis of Major Deposit-Types, District Metallogeny, the Evolution of Geological Provinces, and Exploration Methods. Vol 5. Edited by W.D. Goodfellow. Geological Association of Canada, Mineral Deposits Division.755–791.
- Nelson, J.L., Colpron, M., and Israel, S. 2013. The Cordillera of British Columbia, Yukon, and Alaska: Tectonics and Metallogeny. In Tectonics, Metallogeny and Discovery: The North American Cordillera and Similar Accretionary Settings. Special Publication, Vol. 17. Edited by M. Colpron, T. Bissig, B.G. Rusk and J.F.H. Thompson. Society of Economic Geologists, 53–103.
- Nelson, J.L., Colpron, M., Piercey, S.J., Dusel-Bacon, C., Murphy, D.C., and Roots, C.F. 2006. Paleozoic Tectonic and Metallogenic Evolution of the Pericratonic Terranes in Yukon, northern British Columbia and eastern Alaska. In Paleozoic Evolution and Metallogeny of Pericratonic Terranes at the Ancient Pacific Margin of North America, Canadian and Alaskan Cordillera. Edited by M. Colpron and J.L. Nelson. Geological Association of Canada, Special Paper 45. pp. 323–360.
- Nelson, J.L., van Straaten, B., and Friedman, R. 2022. Latest Triassic–early Jurassic Stikine–Yukon–Tanana terrane collision and the onset of accretion in the Canadian Cordillera: Insights from Hazelton group detrital zircon provenance and arc-back-arc configuration. *Geosphere*, **18**(2): 670–696. doi:[10.1130/ges02444.1](https://doi.org/10.1130/ges02444.1).
- Niemi, N.A., Buscher, J.T., Spotila, J.A., House, M.A., and Kelley, S.A. 2013. Insights from low-temperature thermochronometry into transpressional deformation and crustal exhumation along the San Andreas fault in the western Transverse Ranges, California. *Tectonics*, **32**: 1602–1622. doi:[10.1002/2013TC003377](https://doi.org/10.1002/2013TC003377).
- O’Sullivan, P.B., and Lane, L.S. 1997. Early Tertiary thermotectonic history of northern Yukon and adjacent Northwest Territories, Arctic Canada. *Canadian Journal of Earth Sciences*, **34**: 1366–1378. doi:[10.1139/e17-109](https://doi.org/10.1139/e17-109).
- Pattison, D.R.M., and Vogl, J.J. 2005. Contrasting sequences of metapelitic mineral-assemblages in the aureole of the tilted Nelson batholith. British Columbia: Implications for phase equilibria and pressure determination in andalusite-sillimanite-type sequences. *The Canadian Mineralogist*, **43**: 51–88. doi:[10.2113/gscanmin.43.1.51](https://doi.org/10.2113/gscanmin.43.1.51).
- Powell, J., Schneider, D., Stockli, D., and Fallas, K. 2016. Zircon (U-Th)/He thermochronology of Neoproterozoic strata from the Mackenzie Mountains, Canada: Implications for the Phanerozoic exhumation and deformation history of the northern Canadian Cordillera. *Tectonics*, **35**(3): 663–689. doi:[10.1002/2015tc003989](https://doi.org/10.1002/2015tc003989).
- Price, P.B., and Walker, R.M. 1963. Fossil tracks of charged particles in mica and the age of minerals. *Journal of Geophysical Research*, **68**(16): 4847–4862. doi:[10.1029/jz068i016p04847](https://doi.org/10.1029/jz068i016p04847).
- Rasmussen, K. 2013. The timing, composition, and petrogenesis of syn-to post-accretionary magmatism in the Northern Cordilleran Miogeocline, Eastern Yukon and Southwestern Northwest Territories. Ph.D. dissertation. University of British Columbia.
- Reiners, P.W., Spell, T.L., Nicolescu, S., and Zanetti, K.A. 2004. Zircon (U-Th)/He thermochronometry: He diffusion and comparisons with  $^{40}\text{Ar}/^{39}\text{Ar}$  dating. *Geochimica et Cosmochimica Acta*, **68**(8): 1857–1887. doi:[10.1016/j.gca.2003.10.021](https://doi.org/10.1016/j.gca.2003.10.021).
- Roots, E.F., Green, L.H., Roddick, J.A., and Blusson, S.L. 1966. Geology, Frances Lake, Yukon Territory and District of Mackenzie. Geological Survey of Canada, Preliminary Map 6-1966. Scale 1, pp. 253–440.
- Spotila, J.A., Farley, K.A., and Sieh, K. 1998. Uplift and erosion of the San Bernardino Mountains associated with transpression along the San Andreas fault, California, as constrained by radiogenic helium thermochronometry. *Tectonics*, **17**: 360–378. doi:[10.1029/98TC00378](https://doi.org/10.1029/98TC00378).
- Spotila, J.A., Farley, K.A., Yule, J.D., and Reiners, P.W. 2001. Near-field transpressive deformation along the San Andreas Fault Zone in Southern California, based on exhumation constrained by (U-Th)/He dating. *Journal of Geophysical Research: Solid Earth*, **106**(B12): 30909–30922. doi:[10.1029/2001jb000348](https://doi.org/10.1029/2001jb000348).
- Spotila, J.A., Mason, C.C., Valentino, J.D., and Cochran, W.J. 2020. Constraints on rock uplift in the eastern Transverse Ranges and northern Peninsular Ranges and implications for kinematics of the San Andreas fault in the Coachella Valley, California, USA. *Geosphere*, **16**: 723–750. doi:[10.1130/GES02160.1](https://doi.org/10.1130/GES02160.1).
- Spotila, J.A., Niemi, N., Brady, R., House, M., Buscher, J., and Oskin, M. 2007. Long-term continental deformation associated with transpressive plate motion: The San Andreas fault. *Geology*, **35**: 967–970. doi:[10.1130/G23816A.1](https://doi.org/10.1130/G23816A.1).
- Staples, R.D., Gibson, H.D., Colpron, M., and Ryan, J.J. 2016. An orogenic wedge model for diachronous deformation, metamorphism, and exhumation in the hinterland of the northern Canadian Cordillera. *Lithosphere*, **8**: 165–184. doi:[10.1130/L472.1](https://doi.org/10.1130/L472.1).
- Tollefson, K.T., Larson, K.P., Cleven, N.R., and Moynihan, D.P. 2023) Dating ductile deformation by *in-situ* Rb-Sr dating: Examples from the d’Abbadie and Shannon Faults, Yukon, Canada. Cordilleran Tectonics Workshop, Whitehorse, Yukon.
- Vice, L., Gibson, H.D., and Israel, S. 2020. Late Cretaceous to Paleocene Tectonometamorphic Evolution of the Blanchard River Assemblage, southwest Yukon: New Insight into the Terminal Accretion of Insular Terranes in the Northern Cordillera. *Lithosphere*, **2020**(1). doi:[10.2113/2298288](https://doi.org/10.2113/2298288).

- Whipp, D.M., Kellett, D.A., Coutand, I., and Ketcham, R.A. 2022. Short communication: Modeling competing effects of cooling rate, grain size, and radiation damage in low-temperature thermochronometers. *Geochronology*, **4**(1): 143–152. doi:[10.5194/gchron-4-143-2022](https://doi.org/10.5194/gchron-4-143-2022).
- White, D., Colpron, M., and Buffett, G. 2012. Seismic and geological constraints on the structure and hydrocarbon potential of the northern Whitehorse Trough, Yukon, Canada. *Bulletin of Canadian Petroleum Geology*, **60**(4): 239–255. doi:[10.2113/gscpgbull.60.4.239](https://doi.org/10.2113/gscpgbull.60.4.239).
- Wildman, M., Brown, R., Beucher, R., Persano, C., Stuart, F., Gallagher, K., et al. 2016. The chronology and tectonic style of landscape evolution along the elevated Atlantic continental margin of South Africa re-solved by joint apatite fission track and (U-Th-Sm)/He thermochronology. *Tectonics*, **35**(3): 511–545. doi:[10.1002/2015tc004042](https://doi.org/10.1002/2015tc004042).
- Woodcock, N.H., and Fischer, M. 1986. Strike-slip duplexes. *Journal of Structural Geology*, **8**: 725–735. doi:[10.1016/0191-8141\(86\)90021-0](https://doi.org/10.1016/0191-8141(86)90021-0).
- Yukon Geological Survey. 2022. Yukon digital bedrock geology. Yukon Geological Survey. Available from <https://data.geology.gov.yk.ca/Compilation/3> [accessed 13 December 2024].
- Zeitler, P.K., Herczeg, A.L., McDougall, I., and Honda, M. 1987. U-Th-He Dating of Apatite: A Potential Thermochronometer. *Geochimica et Cosmochimica Acta*, **51**(10): 2865–2868. doi:[10.1016/0016-7037\(87\)90164-5](https://doi.org/10.1016/0016-7037(87)90164-5).